



**University of
Sunderland**

Elkady, Mustafa, Elmarakbi, Ahmed, MacIntyre, John and Al-Hariri, Mohammad (2017) Collision mitigation and vehicle transportation safety using integrated vehicle dynamics control systems. *Journal of Traffic and Transportation Engineering (English Edition)*, 4 (1). pp. 41-60. ISSN 2095-7564

Downloaded from: <http://sure.sunderland.ac.uk/id/eprint/7098/>

Usage guidelines

Please refer to the usage guidelines at <http://sure.sunderland.ac.uk/policies.html> or alternatively contact sure@sunderland.ac.uk.

1 Original research paper

2

3 **Collision mitigation and vehicle transportation safety** 4 **using integrated vehicle dynamics control systems**

5

6 Mustafa Elkady ^{a,b}, Ahmed Elmarakbi ^{c,*}, John MacIntyre ^c, Mohammed Alhariri ^c

7

8 ^a *School of Engineering, Lebanese International University, Beirut, Lebanon*

9 ^b *Faculty of Engineering, Ain Shams University, Cairo, Egypt*

10 ^c *School of Engineering, Faculty of Engineering and Advanced Manufacturing, University of Sunderland,*

11 *Sunderland, SR6 0DD, UK*

12 **Highlights**

- 13 • Integrated vehicle dynamics control systems for collisions improvement
- 14 • Development of a new dynamics/crash mathematical model for vehicle collisions
- 15 • Development of a new occupant- based lumped mass-spring-damper mathematical model
- 16 • Vehicle response and occupant behaviour are captured and analysed accurately

17

18 **Abstract**

19 The aim of this paper is to investigate the effect of vehicle dynamics control systems
20 (VDCS) on both the collision of the vehicle body and the kinematic behaviour of the
21 vehicle's occupant in case of offset frontal vehicle-to-vehicle collision. A unique
22 6-degree-of-freedom (6-DOF) vehicle dynamics/crash mathematical model and a
23 simplified lumped mass occupant model are developed. The first model is used to define
24 the vehicle body crash parameters and it integrates a vehicle dynamics model with a
25 vehicle front-end structure model. The second model aims to predict the effect of VDCS on

26 the kinematics of the occupant. It is shown from the numerical simulations that the vehicle
27 dynamics/crash response and occupant behaviour can be captured and analysed quickly
28 and accurately. Furthermore, it is shown that the VDCS can affect the crash characteristics
29 positively and the occupant behaviour is improved.

30

31

32

33 **Keywords:**

34 Vehicle transportation safety; Collision mitigation; Vehicle dynamics and control; Mathematical
35 modelling; Occupant kinematics.

36

*Corresponding author. Tel.: +44 191 515 3877.
E-mail address: ahmed.elmarakbi@sunderland.ac.uk (A. Elmarakbi).

37 1 Introduction

38 Vehicle dynamics control systems (VDCS) exist on the most modern vehicles and play important roles
39 in vehicle ride, stability, and safety. For example, anti-lock brake system (ABS) is used to allow the
40 vehicle to follow the desired steering angle while intense braking is applied (Yu et al., 2002; Bang et al.,
41 2001). In addition, the ABS helps reducing the stopping distance of a vehicle compared to the
42 conventional braking system (Celentano et al., 2003; Pasillas-Lépine, 2006). The active suspension
43 control system (ASC) is used to improve the quality of the vehicle ride and reduce the vertical
44 acceleration (Yue et al., 1988; Alleyne and Hedrick, 1995). From the view of vehicle transportation
45 safety, nowadays, occupant safety becomes one of the most important research areas and the
46 automotive industry increased their efforts to enhance the safety of vehicles. Seat belts, airbags, and
47 advanced driver assistant systems (ADAS) are used to prevent a vehicle crash or mitigate vehicle
48 collision when a crash occurs.

49 The most well-known pre-collision method is the advance driver assistant systems (ADAS). The aim
50 of ADAS is to mitigate and avoid vehicle frontal collisions. The main idea of ADAS is to collect data from
51 the road (i.e. traffic lights, other cars distances and velocities, obstacles, etc.) and transfer this
52 information to the driver, warn the driver in danger situations and aid the driver actively in imminent
53 collision (Seiler et al., 1998; Gietelink et al., 2006). There are different actions may be taken when these
54 systems detect that the collision is unavoidable. For example, to help the driver actively, the braking
55 force can be applied in imminent collision (Jansson et al., 2002), in addition, the brake assistant system
56 (BAS) (Tamura et al., 2001) and the collision mitigation brake system (CMBS) (Sugimoto and Sauer,
57 2005) were used to activate the braking instantly based on the behaviour characteristics of the driver,
58 and relative position of the most dangerous other object for the moment.

59 Vehicle crash structures are designed to be able to absorb the crash energy and control vehicle
60 deformations, therefore simple mathematical models are used to represent the vehicle front structure
61 (Emori, 1968). In this model, the vehicle mass is represented as a lumped mass and the vehicle
62 structure is represented as a spring in a simple model to simulate a frontal and rear-end vehicle collision
63 processes. Also, other analyses and simulations of vehicle-to-barrier impact using a simple mass spring

64 model were established by Kamal (1970) and widely extended by Elmarakbi and Zu (2005, 2007) to
65 include smart-front structures. To achieve enhanced occupant safety, the crash energy management
66 system was explored by Khattab (2010). This study, using a simple lumped-parameter model,
67 discussed the applicability of providing variable energy-absorbing properties as a function of the impact
68 speed.

69 In terms of the enhancing crash energy absorption and minimizing deformation of the vehicle's
70 structure, a frontal structure consisting of two special longitudinal members was designed (Witteman
71 and Kriens, 1998; Witteman, 1999). This longitudinal member system was divided to two separate
72 systems: the first, called the crushing part, guarantees the desired stable and efficient energy
73 absorption; the other, called the supporting part, guarantees the desired stiffness in the transverse
74 direction. For high crash energy absorption and weight efficiency, new multi-cell profiles were
75 developed (Kim, 2002). Various design aspects of the new multi-cell members were investigated and
76 the optimization was carried out as an exemplary design guide.

77 The vehicle body pitch and drop at frontal impact is the main reason for the unbelted driver neck and
78 head injury (Chang et al., 2006). Vehicle pitch and drop are normally experienced at frontal crash tests.
79 They used a finite element (FE) method to investigate the frame deformation at full frontal impact and
80 discussed the cause and countermeasures design for the issue of vehicle body pitch and drop. It found
81 that the bending down of frame rails caused by the geometry offsets of the frame rails in vertical
82 direction during a crash is the key feature of the pitching of the vehicle body.

83 The effect of vehicle braking on the crash and the possibility of using vehicle dynamics control
84 systems to reduce the risk of incompatibility and improve the crash performance in frontal
85 vehicle-to-barrier collision were investigated (Hogan and Manning, 2007). They proved that there was a
86 slight improvement of the vehicle deformation once the brakes were applied during the crash. A
87 multi-body vehicle dynamic model using ADAMS software, alongside with a simple crash model was
88 generated in order to study the effects of the implemented control strategy.

89 Their study showed that the control systems were not able to significantly affect the vehicle dynamics
90 in the offset barrier impact. In addition, it was found that in offset vehicle-to-vehicle rear-end collision,
91 the ABS or direct yaw control (DYC) systems can stabilise the vehicle. However, these control systems

92 affected each other and cannot work together at the same time.

93 The behaviour of a vehicle at high-speed crashes is enhanced by using active vehicle dynamics
94 control systems (Elkady and Elmarakbi, 2012). A 6-degree-of-freedom (6-DOF) mathematical model
95 was developed to carry out this study. In this model, vehicle dynamics was studied together with a
96 vehicle crash structural dynamics and a validation of the vehicle crash structure of the proposed model
97 was achieved. Four different cases of VDCS were applied to the model to predict the most effective one.
98 An extension to this study, an occupant model has been developed and the effect of VDCS on the
99 occupant kinematics has been analysed (Elkady and Elmarakbi, 2012).

100 The main aim of this research is to investigate the effect of the VDCS on vehicle collision mitigation,
101 enhance vehicle crash characteristics, and improve occupant biodynamics responses in case of 50%
102 vehicle-to-vehicle offset crash scenario. For that purpose, different seven cases of VDCS are applied to
103 the vehicle model, there are three new cases which are not mentioned in the previous publications.

104 **2 Methodology**

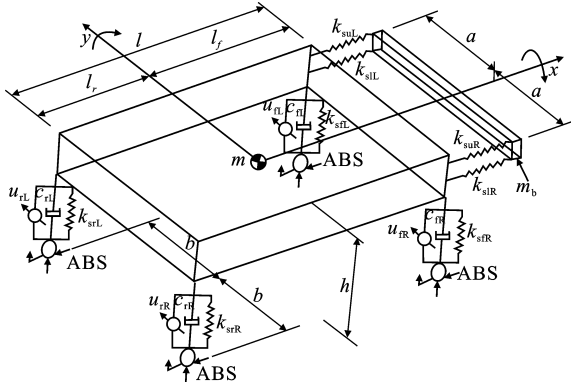
105 A vehicle frontal collision can be divided into two main stages, the first one is a primary impact, and the
106 second one is a secondary impact. The primary impact indicates the collision between the front-end
107 structure of the vehicle and an obstacle (another vehicle in this paper). The secondary impact is the
108 interaction between the occupant and the restraint system and/or the vehicle interior due to vehicle
109 collisions.

110 *2.1 Vehicle dynamics/crash model*

111 Using mathematical models in crash simulation is useful at the first design concept because rapid
112 analysis is required at this stage. In addition, the well-known advantage of mathematical modelling
113 provides a quick simulation analysis compared with FE models. In this paper, a 6-DOF vehicle
114 dynamics/crash mathematical model, shown in Fig. 1(a), has been developed to optimise the VDCS,
115 which will be embedded in the control unit, in impending impact at offset vehicle-to-vehicle crash
116 scenarios for vehicle collision mitigation. The ABS and the ASC systems are co-simulated with a full car
117 vehicle dynamic model and integrated with a front-end structure. It is worthwhile mentioning that vehicle

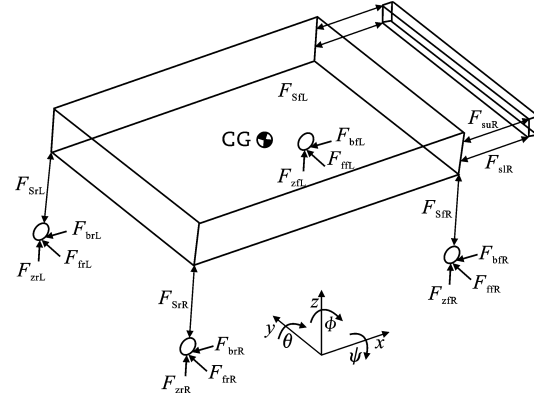
118 components, which significantly affect the dynamics of a frontal impact, are modelled by lumped
 119 masses and nonlinear springs.

120 (a)



121

(b)



122 **Fig. 1** Mathematical model. (a) 6-DOF vehicle dynamics/crash mathematical model. (b) Free body diagram of the mathematical model.

123 In this full-car model, the vehicle body is represented by lumped mass m and it has a translational
 124 motion in longitudinal direction (x axis), translational motion on vertical direction (z axis), pitching motion
 125 (around y axis), rolling motion (around x axis), and yawing motion in case of offset collision (around z
 126 axis at the point of impact). Four spring/damper units are used to represent the conventional vehicle
 127 suspension systems. Each unit has a spring stiffness k_s and a damping coefficient c . The subscripts f, r,
 128 R and L denote the front, rear, right and left wheels, respectively. The ASC system is co-simulated with
 129 the conventional suspension system to add or subtract an active force element u . The ABS is
 130 co-simulated with the mathematical model using a simple wheel model. The unsprung masses are not
 131 considered in this model and it is assumed that the vehicle moves in a flat-asphalted road, which means
 132 that the vertical movement of the tyres and road vertical forces can be neglected.

133 To represent the front-end structure of the vehicle, four non-linear springs with stiffness k_s are
 134 proposed: two springs represent the upper members (rails) and two springs represent lower members of
 135 the vehicle frontal structure. The subscript u denotes the upper rails while the subscript l denotes the
 136 lower rails. The bumper of the vehicle is represented by a lumped mass m_b and it has a longitudinal
 137 motion in the x direction and rotational motion for the non-impacted side of each bumper.

138 The general dimensions of the model are shown in Fig. 1(a), where l_f , l_r , l and h represent the
 139 longitudinal distance between the vehicle's CG and front wheels, the longitudinal distance between the

140 CG and rear wheels, the wheel base and the high of the CG from the ground, respectively. a is the
141 distance between the centre of the bumper and the right/left frontal springs; b is the distance between
142 the CG and right/left wheels.

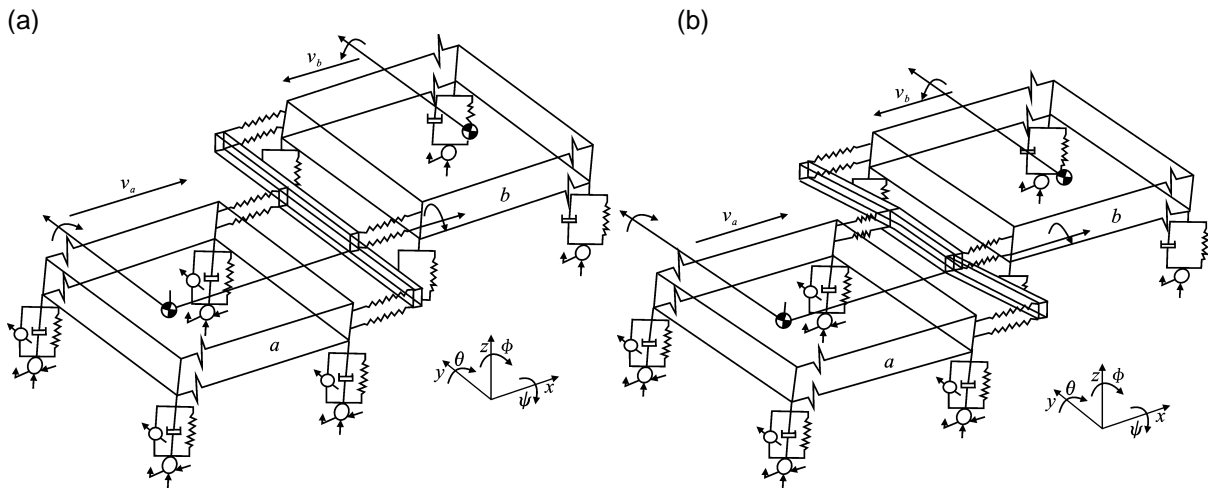
143 The free body diagram of the mathematical model is shown in Fig. 1(b), which represents the different
144 internal and external forces applied on the vehicle body. F_s , F_S , F_b , F_z and F_f are front-end non-linear
145 spring forces, vehicle suspension forces, braking forces, normal forces and friction forces between the
146 tyres and the road due to vehicle yawing, respectively.

147 2.1.1 *Equations of motion of vehicle-to-vehicle crash scenario*

148 The model in the case of offset frontal vehicle-to-barrier is thirteen DOF namely longitudinal and vertical
149 movements, pitching, rolling and yawing motions for each vehicle body, the longitudinal movement of
150 the two bumpers as one part, and the rotational motion for the non-impacted side of each bumper. The
151 two bumpers of each vehicle are considered as lumped masses, and dealt as one mass to transfer the
152 load from one vehicle to another. Figs. 2(a) and 2(b) show the vehicle model before and after collision in
153 case of offset frontal vehicle-to-vehicle crash scenario. The equations of motion of the mathematical
154 model shown in Fig. 2 are developed to study and predict the dynamic response of the primary impact of
155 offset vehicle-to-vehicle crash scenario. Figs. 3(a) and 3(b) are used to describe the deformation of the
156 front springs due to vehicle pitching around its CG and vehicle yawing around the point of impact for the
157 two vehicles, respectively. Fig. 1 is also used to derive the equations of motion of the two vehicle
158 models. The detailed equations of motion were created in a previous study by the authors (Elmarakbi et
159 al., 2013).

160
161
162
163
164
165
166
167
168
169
170
171
172

173
174
175

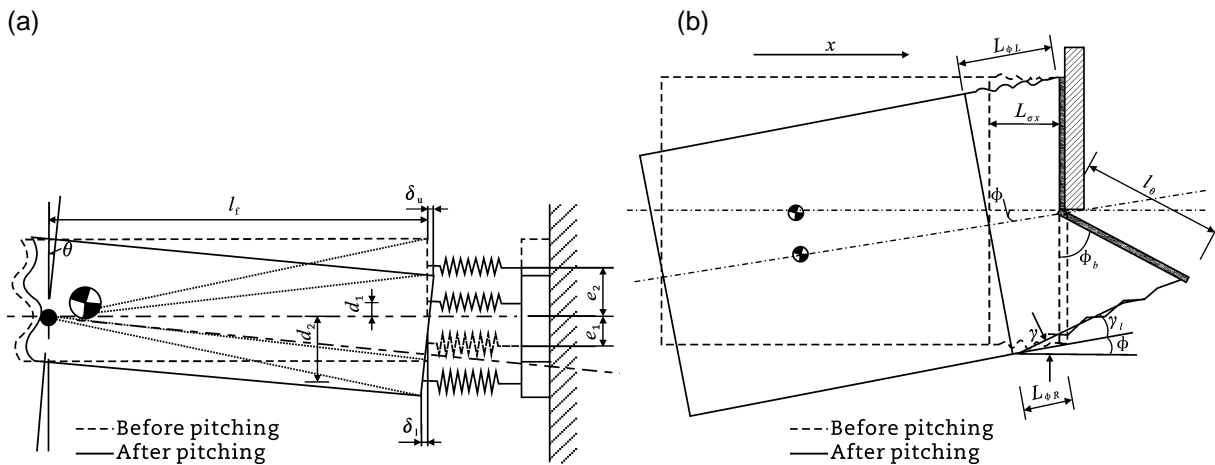


176
177

Fig. 2 vehicle models (offset frontal impact). (a) Before crash. (b) After crash.

178
179

180



181

182

183

Fig. 3 The front-end deformation before and after pitching. (a) For vehicle pitching. (b) For vehicle yawing.

184

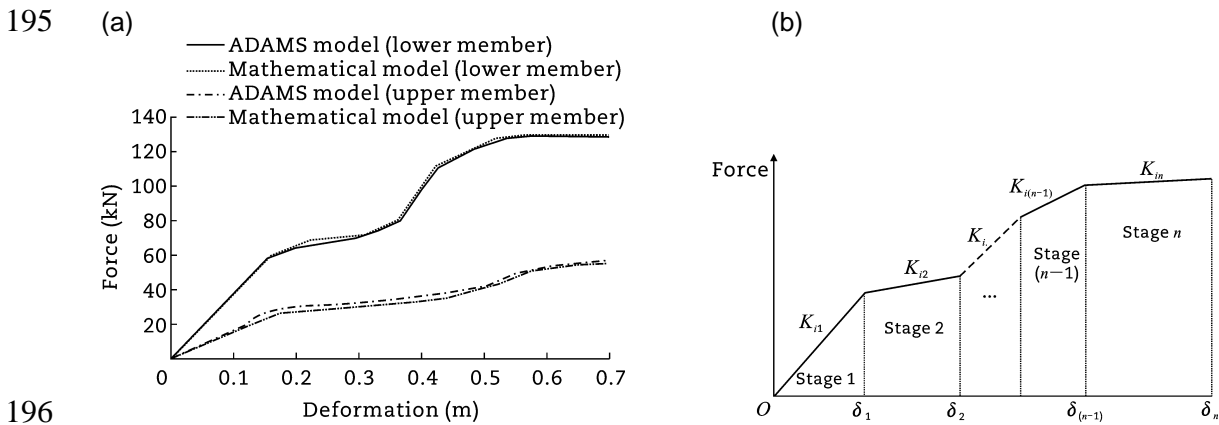
2.1.2 Forces applied to the vehicle

185

There are different types of forces which are applied on the vehicle body. These forces are generated by crushing the front-end structure, conventional suspension system due to the movement of the vehicle body and the active control systems such as the ABS and ASC. The free body diagram shown in Fig. 1(b) illustrates these different forces and their directions.

188

189 To simulate the upper and lower members of the vehicle front-end structure, multi-stage piecewise
 190 linear force-deformation spring characteristics are considered. The non-linear springs used in the
 191 multi-body model ADAMS (Hogan and Manning, 2007) are taken to generate the n stage piecewise
 192 spring's characteristics as shown in Fig. 4(a), while the general relationship between the force and the
 193 deflection, Fig. 4(b), is used to calculate the force of the vehicle's front-end. The suspension forces of
 194 the vehicle body are also calculated.



196
 197 **Fig. 4** Force deformation characteristics. (a) For upper and lower rails. (b) General piecewise.

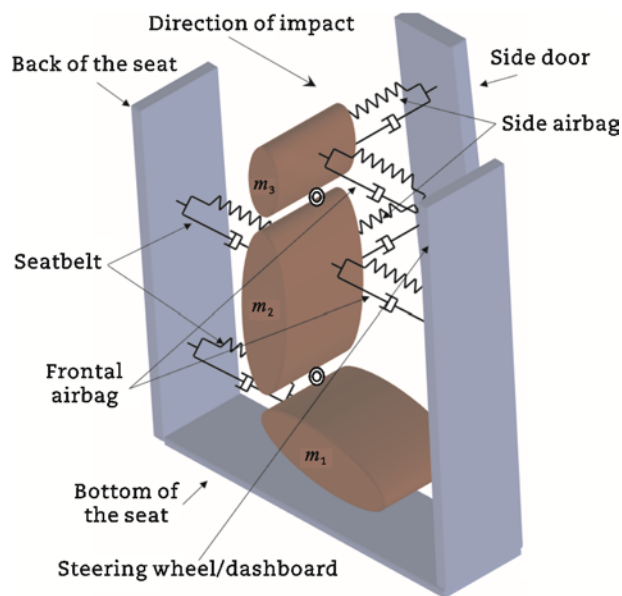
198 The detailed equations of these forces and the validation of the vehicle dynamics–crash model was
 199 established in a previous study by the authors (Elkady and Elmarakbi, 2012). The validation is
 200 performed to ensure the validity of the model and is accomplished by comparing the mathematical
 201 model results with real test data and the results of the former ADAMS model. The validation showed that
 202 the mathematical model results are well matched with the other results.

203 **2.2 Multi-body occupant model**

204 In this section, occupant biodynamics is considered by modelling the occupant mathematically in order
 205 to be integrated with the vehicle mathematical model. The occupant model is proposed to be three-body
 206 model to capture its dynamic response, rotational events of the chest and head, due to different crash
 207 scenarios. The restraint system consists of seat belt, front and side airbags is presented by different
 208 spring-damper systems.

209 The occupant biodynamic model shown in Fig. 5 is developed in this study to evaluate the occupant

210 kinematic behaviour in full and offset frontal crash scenarios. The human body model consists of three
 211 bodies with masses m_1 , m_2 and m_3 . The first body (lower body/pelvis) with mass m_1 , represents the legs
 212 and the pelvic area of the occupant and it is considered to have a translation motion in the longitudinal
 213 direction and rotation motions (pitching, rolling and yawing) with the vehicle body. The second body
 214 (middle body/chest), with mass m_2 , represents the occupant's abdominal area, the thorax area and the
 215 arms, and it is considered to have a translation motion in the longitudinal direction and a rotation motion
 216 around the pivot between the lower and middle bodies (pivot 1). The third body (upper body/head), with
 217 mass m_3 , represents the head and neck of the occupant and it is considered to have a translation motion
 218 in the longitudinal direction and a rotational motion around the pivot between the middle and upper
 219 bodies (pivot 2).



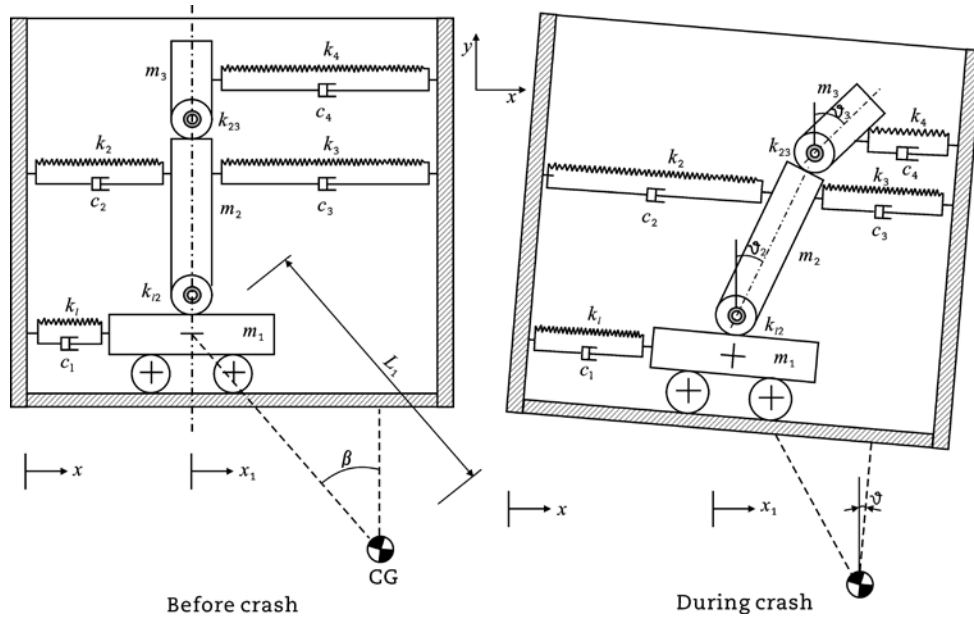
220
 221 **Fig. 5** Multi-body occupant model.

222 A rotational coil spring is proposed at each pivot to represent the joint stiffness between the pelvic
 223 area and the abdominal area and between the thorax area and the neck/head area. The seatbelt is
 224 represented by two linear spring-damper units between the compartment and the occupant. The frontal
 225 and side airbags are each represented by two linear spring-damper units.

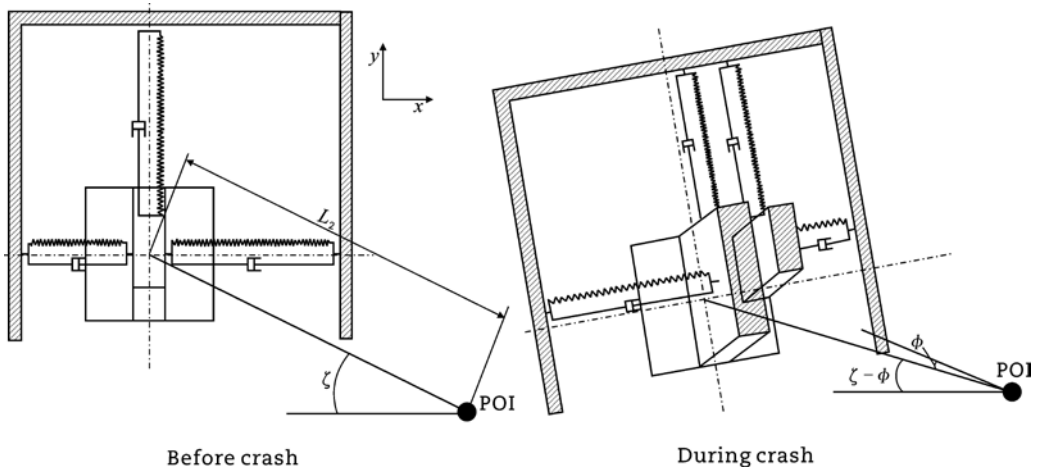
226 **2.2.1 Equation of motion (EOM) of the human body model**

227 Figs. 6 (a), (b), and (c) show the side, top and front views of the occupant model, respectively. For each
 228 figure, the positions of the occupant's three bodies are illustrated before and after the crash. Lagrange's
 229 equations are used to describe the general motions of the multi-body human model.

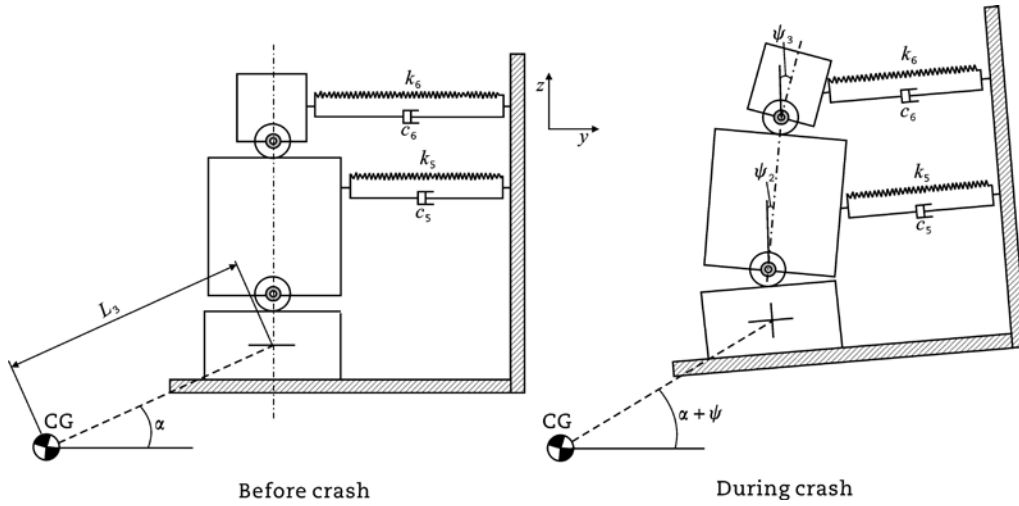
230 (a)



231 (b)
 232



233 (c)
 234



235
236 **Fig. 6** Occupant model. (a) Side view. (b) Top view (POI is point of impact). (c) Frontal view.

237 The general motions of the multi-body human model are described using Lagrange's equations as
238 follows

239
$$\frac{d}{dt} \left(\frac{\partial E}{\partial \dot{x}_1} \right) - \frac{\partial E}{\partial x_1} + \frac{\partial V}{\partial x_1} + \frac{\partial D}{\partial \dot{x}_1} = 0 \quad (1)$$

240
$$\frac{d}{dt} \left(\frac{\partial E}{\partial \dot{\theta}_2} \right) - \frac{\partial E}{\partial \theta_2} + \frac{\partial V}{\partial \theta_2} + \frac{\partial D}{\partial \dot{\theta}_2} = 0 \quad (2)$$

241
$$\frac{d}{dt} \left(\frac{\partial E}{\partial \dot{\theta}_3} \right) - \frac{\partial E}{\partial \theta_3} + \frac{\partial V}{\partial \theta_3} + \frac{\partial D}{\partial \dot{\theta}_3} = 0 \quad (3)$$

242
$$\frac{d}{dt} \left(\frac{\partial E}{\partial \dot{\psi}_2} \right) - \frac{\partial E}{\partial \psi_2} + \frac{\partial V}{\partial \psi_2} + \frac{\partial D}{\partial \dot{\psi}_2} = 0 \quad (4)$$

243
$$\frac{d}{dt} \left(\frac{\partial E}{\partial \dot{\psi}_3} \right) - \frac{\partial E}{\partial \psi_3} + \frac{\partial V}{\partial \psi_3} + \frac{\partial D}{\partial \dot{\psi}_3} = 0 \quad (5)$$

244 where E , V and D are the kinetic energy, potential energy and the Rayleigh dissipation function of the
245 system, respectively. x_1 , θ_2 , θ_3 , ψ_2 and ψ_3 are the longitudinal movement of the occupant's lower
246 body, the rotational angle of the occupant's middle body about y axis, the rotational angle of the
247 occupant's upper body about y axis, the rotational angle of the occupant's middle body about x axis and

248 the rotational angle of the occupant's upper body about x axis, respectively. Hence, \dot{x}_1 , $\dot{\theta}_2$, $\dot{\theta}_3$, $\dot{\psi}_2$ and
 249 $\dot{\psi}_3$ are their associated velocities, respectively.

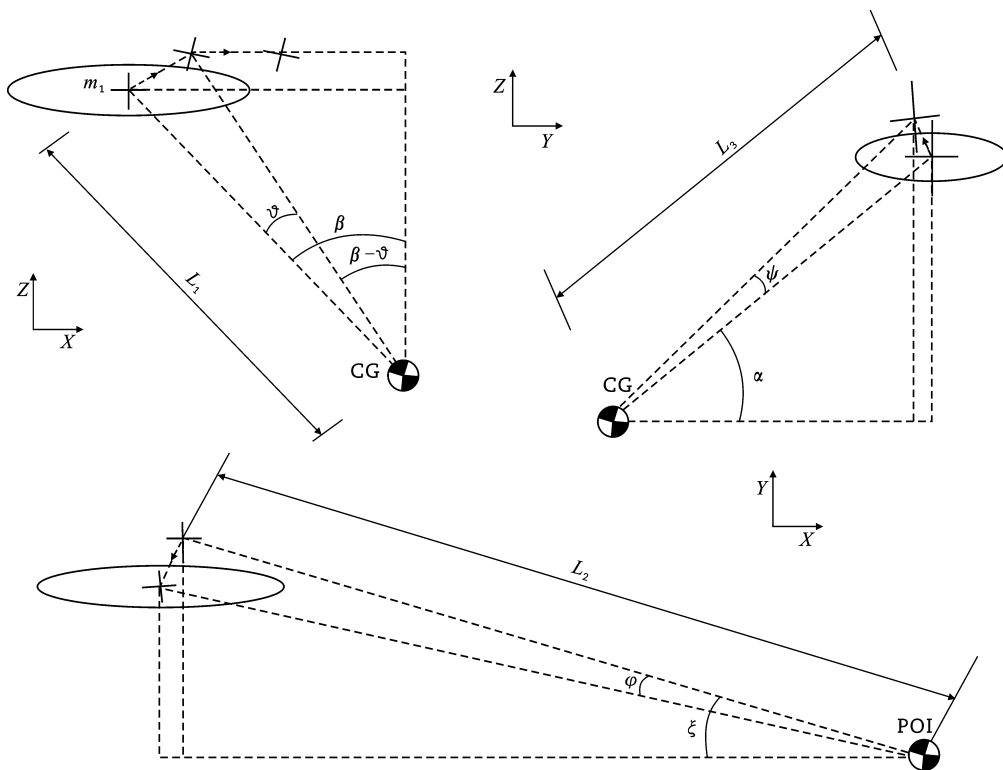
250 The kinetic energy of the system can be written as

$$251 \quad E = \frac{m_1 v_1^2}{2} + \frac{m_2 v_2^2}{2} + \frac{m_3 v_3^2}{2} + \frac{I_1}{2} (\dot{\theta}^2 + \dot{\phi}^2 + \dot{\psi}^2) + \frac{I_2}{2} (\dot{\theta}_2^2 + \dot{\psi}_2^2) + \frac{I_3}{2} (\dot{\theta}_3^2 + \dot{\psi}_3^2) \quad (6)$$

252 where v_1 , v_2 and v_3 are the equivalent velocities of the lower, middle and upper bodies of the occupant,
 253 respectively. I_1 , I_2 and I_3 are the rotational moment of inertia of the lower, middle and upper bodies about
 254 the CG of each body, respectively. It is assumed that the rotational moment of inertia of each body
 255 around x , y and z axes are the same. $\dot{\theta}$, $\dot{\phi}$ and $\dot{\psi}$ represent the vehicle body pitching, yawing and
 256 rolling velocities, respectively. The equivalent velocities of the three bodies of the occupant can be
 257 calculated as follows

$$258 \quad v_1^2 = \dot{X}_{m_1}^2 + \dot{Y}_{m_1}^2 + \dot{Z}_{m_1}^2 \quad (7)$$

259 where the displacement of the lower body in x direction can be calculated using Fig. 7 as



260

261 **Fig. 7** A schematic diagram of the occupant's lower body movement during impact.

262
$$X_{m_1} = x_1 + L_1[\sin(\beta) - \sin(\beta - \theta)] - L_2[\cos(\zeta - \phi) - \cos(\zeta)] \quad (8)$$

263 The velocity of the lower body in x direction can be written as

264
$$\dot{X}_{m_1} = \dot{x}_1 + L_1\dot{\theta}\cos(\beta - \theta) - L_2\dot{\phi}\sin(\zeta - \phi) \quad (9)$$

265 The displacement and velocity of the lower body in y direction can be calculated as

266
$$Y_{m_1} = L_2[\sin(\zeta) - \sin(\zeta - \phi)] + L_3[\cos(\alpha) - \cos(\alpha + \psi)] \quad (10)$$

267
$$\dot{Y}_{m_1} = L_2\dot{\phi}\cos(\zeta - \phi) + L_3\dot{\psi}\sin(\alpha + \psi) \quad (11)$$

268 the displacement and velocity of the lower body in y direction can be calculated as

269
$$Z_{m_1} = z + L_1[\cos(\beta - \theta) - \cos(\beta)] + L_3[\sin(\alpha + \psi) - \sin(\alpha)] \quad (12)$$

270
$$\dot{Z}_{m_1} = L_1\dot{\theta}\sin(\beta - \theta) + L_3\dot{\psi}\cos(\alpha + \psi) \quad (13)$$

271 substituting Eqs. (9), (11) and (13) in Eq. (20), the equivalent velocity of the lower body can be
 272 determined. By repeating the previous steps of these equations (Eqs. (8-13)), the equivalent velocities
 273 of the middle and upper bodies can be calculated.

274 Where X_m is the resultant longitudinal displacement in x direction, Y_m is the resultant vertical
 275 displacement in y direction and Z_m is the resultant vertical displacement. The subscripts 1 is for lower
 276 body, 2 is for middle body and 3 is for upper body. L_1 is the distance from the vehicle's y axis to the lower
 277 body's CG, L_2 is the distance between the point of impact and the CG of the lower body, and L_3 is the
 278 distance from the vehicle's x axis to the lower body's CG. It is assumed that L_1 , L_2 and L_3 are constant
 279 due to the insignificant change of their lengths during the crash. β is ζ , α the angles between the vertical
 280 centreline of the vehicle z axis and the line between the vehicle's y axis and the CG of the lower body (L_1).
 281 ζ is the angle between the longitudinal centreline of the vehicle x axis and the line between the point of
 282 impact and the CG of the lower body (L_2). α is the angle between the vertical centreline of the vehicle z
 283 axis and the line between the vehicle's x axis and the CG of the lower body (L_3).

284 By substituting the equivalent velocities of the three bodies in Eq. (6), the kinetic energy can be
 285 obtained. Using Fig. 6 the potential energy of the system can be written as

$$\begin{aligned}
V = & m_1 g [h + z + L_1 (\cos(\beta - \theta) - \cos(\beta))] + m_2 g [h + z + L_1 (\cos(\beta - \theta) - \\
& \cos(\beta)) + \frac{l_2}{2} \cos(\theta_2) - \frac{l_2}{2} (1 - \cos(\psi_2))] + m_3 g [h + z + L_1 (\cos(\beta - \theta) - \\
286 & \cos(\beta)) + l_2 \cos(\theta_2) - l_2 (1 - \cos(\psi_2)) + \frac{l_3}{2} \cos(\theta_3) - \frac{l_3}{2} (1 - \cos(\psi_3))] + \\
& \frac{1}{2} [F_{k1} \delta_1 + F_{k2} \delta_2 + F_{k3} \delta_3 + F_{k4} \delta_4 + F_{k5} \delta_5 + F_{k6} \delta_6 + F_{k12\psi} \delta_{12\theta} + F_{k12\theta} \delta_{12\psi} + \\
& F_{k23\theta} \delta_{23\theta} + F_{k23\psi} \delta_{23\psi}] \tag{14}
\end{aligned}$$

287 where h is the vehicle's CG height and z is the vertical displacement of the vehicle body. $F_{k1}, F_{k2}, F_{k3}, F_{k4},$
288 F_{k5} and F_{k6} are the forces generated from the lower seatbelt spring, the upper seatbelt spring, the lower
289 frontal airbag spring, the upper frontal airbag spring, the lower side airbag spring, the upper side airbag
290 spring, respectively. $F_{k12\theta}$ and $F_{k12\psi}$ are the forces generated from the rotational spring between the
291 middle and lower body around y and x axes, respectively. $F_{k23\theta}$ and $F_{k23\psi}$ are the forces generated from
292 the rotational spring between the upper and middle body around y and x axes, respectively. $\delta_1, \delta_2, \delta_3,$
293 δ_4, δ_5 and δ_6 represent the total deflection of the lower seatbelt spring, of the upper seatbelt spring, of
294 the lower frontal airbag spring, of the upper frontal airbag spring, of the lower side airbag spring, of the
295 upper side airbag spring, respectively. $\delta_{12\theta}$ and $\delta_{12\psi}, \delta_{23\theta}$ and $\delta_{23\psi}$ are the deflection of the
296 rotational spring between the lower and middle body around y and x axes and the deflection of the
297 rotational spring between the middle and upper body around y and x axes, respectively.

298 The Rayleigh dissipation function can be written as follows

$$299 \quad D = \frac{1}{2} [F_{c1} \dot{\delta}_1 + F_{c2} \dot{\delta}_2 + F_{c3} \dot{\delta}_3 + F_{c4} \dot{\delta}_4 + F_{c5} \dot{\delta}_5 + F_{c6} \dot{\delta}_6] \tag{15}$$

300 where $F_{c1}, F_{c2}, F_{c3}, F_{c4}, F_{c5}$ and F_{c6} are the forces generated from the lower seatbelt, the upper seatbelt,
301 the lower frontal airbag, the upper frontal airbag, the lower side airbag, and the upper side airbag
302 dampers, respectively. $\dot{\delta}_1, \dot{\delta}_2, \dot{\delta}_3, \dot{\delta}_4, \dot{\delta}_5,$ and $\dot{\delta}_6$ are the associated velocities of the $\delta_1, \delta_2, \delta_3, \delta_4,$
303 δ_5 and $\delta_6,$ respectively.

304 The forces F_{ki} and F_{ci} (where $i = 1, 2, \dots$) are calculated as

$$305 \quad F_{ki} = k_i \cdot \delta_i \tag{16}$$

306
$$F_{ci} = c_i \dot{\delta}_i \quad (17)$$

307 In order to get the components of the Eqs. (1-5) the differentiations of the kinetic energy, potential
308 energy and Rayleigh dissipation function are determined. To solve these equations, they need to be
309 re-arranged in an integratable form and then rewritten in a matrix form as follows

310
$$A\ddot{\mathbf{B}} = C \quad (18)$$

311 where the $\ddot{\mathbf{B}} = (\ddot{x}_1 \ \ddot{\theta}_2 \ \ddot{\theta}_3 \ \ddot{\psi}_2 \ \ddot{\psi}_3)^T$.

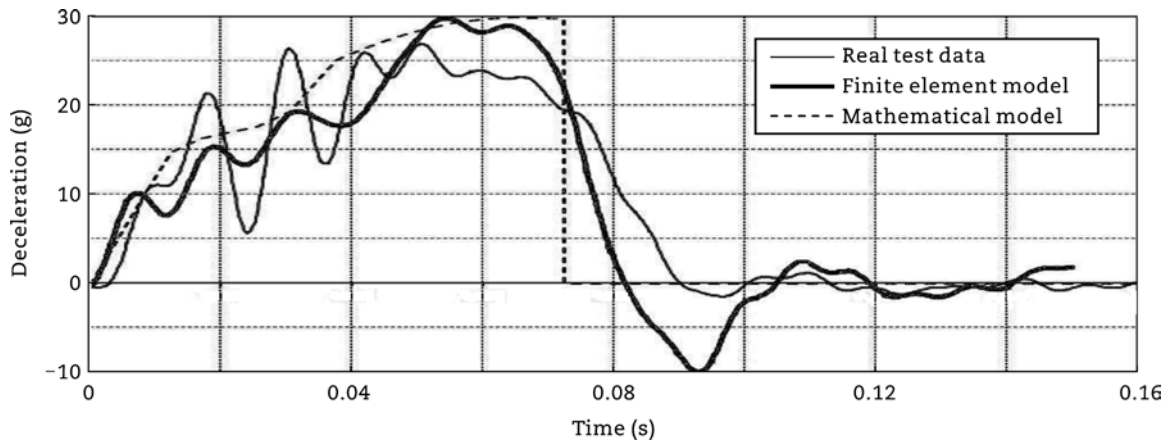
312 The final form then can be written as

313
$$\ddot{\mathbf{B}} = A^{-1}C \quad (19)$$

314 Different occupant bodies' responses (x_1 , θ_2 , θ_3 , ψ_2 and ψ_3) can be determined by solving Eq. (19)
315 numerically.

316 2.2.2 Occupant model validation

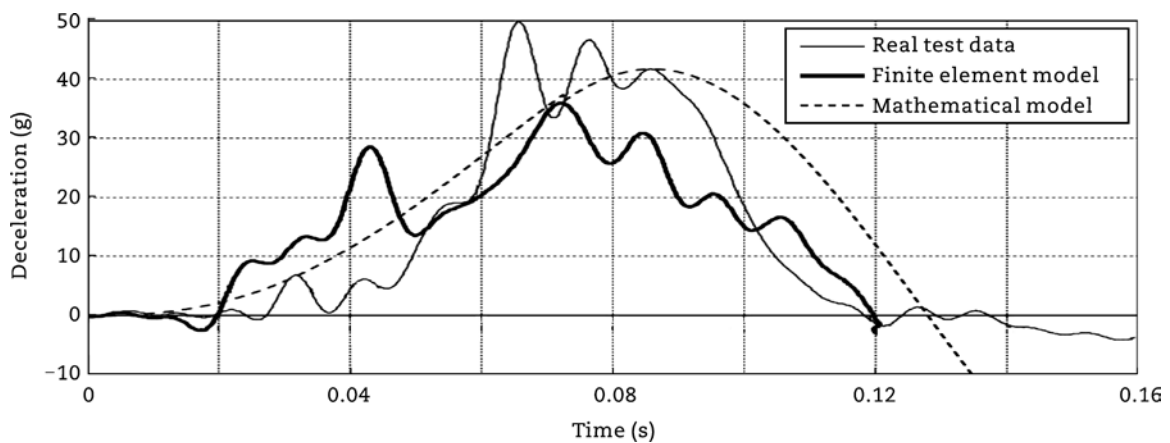
317 The occupant model has been validated by comparing its results with the former finite element human
318 model and crash test. To ensure that the input crash data applied to the dummy and the occupant in the
319 finite element model match the input data in the mathematical model, the vehicle decelerations in all
320 cases (mathematical model, finite element model and real test) are compared as depicted in Fig. 8. The
321 same initial crash conditions are adapted in the mathematical model to be the same as in the FE model
322 and the real test. It is observed that the deceleration of the mathematical model shows outstanding
323 agreement with the real test and the finite element model results with respect to peak values and the
324 timing of the curves.



325
326

327 **Fig. 8** Comparisons of the vehicle body deceleration results among a previous finite model, real test and the mathematical model.

328 Similarly, Fig. 9 shows the chest deceleration-time histories of the real test, finite element and
 329 mathematical models. The values and trends of the three different chest deceleration curves are
 330 well-matched. The maximum deceleration of the occupant chest in the mathematical model is a slightly
 331 lower compared to the real test data, while it is a slightly higher compared to the finite element model. In
 332 addition, there is a small shifting in this peak value compared with the other results. This is due to the
 333 modelling simplification of the airbag used in the mathematical models.

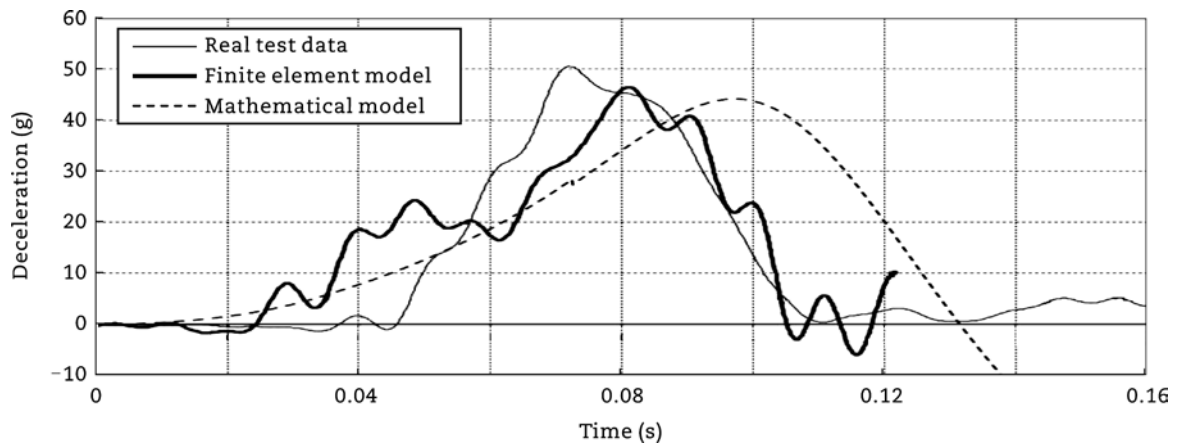


334
335
336
337

Fig. 9 Comparisons of the chest deceleration results among a previous finite element model, a real test and 3-body mathematical model.

338 In the same way, the head deceleration results of the occupant models are presented in Fig. 10.
 339 Although the general trends and slopes of the three different results are well matched, there is a small
 340 difference in the peak value of the mathematical model compared with both finite element and real test
 341 results. A small shifting of the head deceleration peak value is also observed here for both finite element

342 and mathematical models by different values compared with the real test data.



343
344
345
346

Fig. 10 Comparisons of the head deceleration results among a previous finite element model, a real test and a 3-body mathematical model.

347 **3 Numerical simulations**

348 Seven different cases of VDCS are investigated in this section and their associated results are
349 compared with the free rolling case scenario. These different VDCS cases are described as follows.

350 Case 1: free rolling - in this case the vehicle collides with a barrier/vehicle without applying any types
351 of control.

352 Case 2: ABS - in this case the anti-lock braking system is applied before and during the collision.

353 Case 3: ABS + ASC - the ASC system is integrated with the ABS to increase the vertical normal force
354 on the road (Ori et al., 2011) and hence increase the braking force.

355 Case 4: ABS + frontal active suspension control (FASC) - the ASC system is integrated with the ABS
356 on the front wheels only.

357 Case 5: ABS + anti-pitch control (APC) - the APC system is integrated with the ABS using the ACS to
358 keep the vehicle in a horizontal position before the crash by applying an active force element on the front
359 and rear wheels in upward and downward directions, respectively.

360 Case 6: ABS + UPC - in this case, the vehicle is taken a reverse pitching angle before crash using an
361 ASC system.

362 Case 7: ABS DYC - the braking force is used to be applied to individual wheels to reduce the yawing
363 moment of the vehicle body.

364 3.1 Primary impact results

365 The primary impact simulation results for offset vehicle-to-vehicle crash scenario are demonstrated in
366 this section. The values of different parameters used in numerical simulations are given in Table 1
367 (Alleyne, 1997). The effect of the different cases of VDCS on vehicle collision mitigation is also
368 investigated. In addition, the effect of the control systems on the other vehicle (vehicle (b)) is discussed.
369 Figs. 11(a) and (b) show the impacted side of the front-end structure's deformation-time histories for
370 vehicle (a) for all different VDCS cases. It is noticed that the deformation increased to reach its
371 maximum value (different for each case) and then decreased slightly due to front-end springs rebound.
372 The minimum deformation is obtained in the Case 3 when the ASC is applied along with ABS. The
373 maximum reduction of 50 mm is observed in this case and a reduction of 30 mm is shown in Case 6,
374 while a reduction of about 25 mm is obtained in Cases 2, 4 and 5 compared with the free rolling case. On
375 the other hand, Case 7 (ABS + DYC) produced a higher deformation with a total reduction of about 15
376 mm. Although 50 mm is relatively small compared with the total deformation, this reduction may help
377 prevent the compartment to be reached. The integrated control of the ASC with the ABS aims to
378 increase the braking force by increasing the vertical load to obtain a minimum stopping distance. It is
379 worth mentioning that the application of the ASC control system (Case 3) helps reducing the maximum
380 deformation of the front-end structure as shown in Fig. 11. For vehicle (b), the maximum deformation is
381 almost the same with very small and insignificant values for all cases of VDCS, and this means the
382 control systems have no great effect on the front-end deformation of the other vehicle during the offset
383 collision.

384
385
386
387
388
389
390
391
392
393
394
395

396

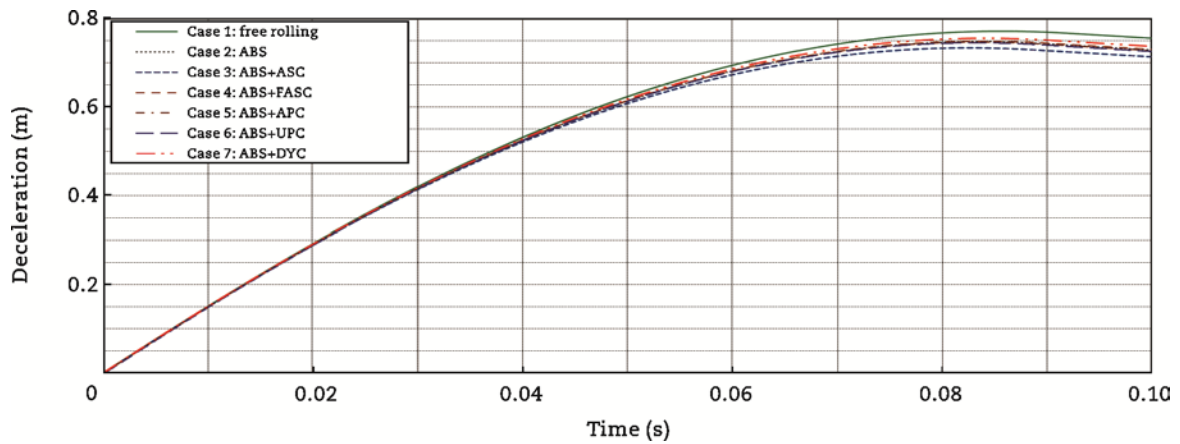
Table 1 Values of the different parameters used in the simulations.

Parameter	m	I_{yy}	I_{xx}	I_{zz}	I_{bzz}	$k_{SfR} = k_{SfL}$	
Value	1200 kg	1490 kg · m ²	350 kg · m ²	1750 kg · m ²	40 kg · m ²	18.25 kN/m	
Parameter	$k_{SfR} = k_{SfL}$	$c_{fR} = c_{fL}$	$c_{rR} = c_{rL}$	l_f	l_r	h	l_a
Value	13.75 kN/m	1100 N.s/m	900 N.s/m	1.185 m	1.58 m	0.452 m	1.2 m
Parameter	l_b			$b_i = b_o$			
Value	0.85 m			0.8 m			

397

398 where I_{yy} , I_{xx} , I_{zz} and I_{bzz} are the moments of inertia of the vehicle body about y , x and z axes and the
 399 moment of inertia of the rotation part of the bumper (the part of the bumper rotated with the
 400 non-impacted side of the vehicle due to offset collisions) about z axis at the point of impact, respectively.

401 (a)



402

403 (b)

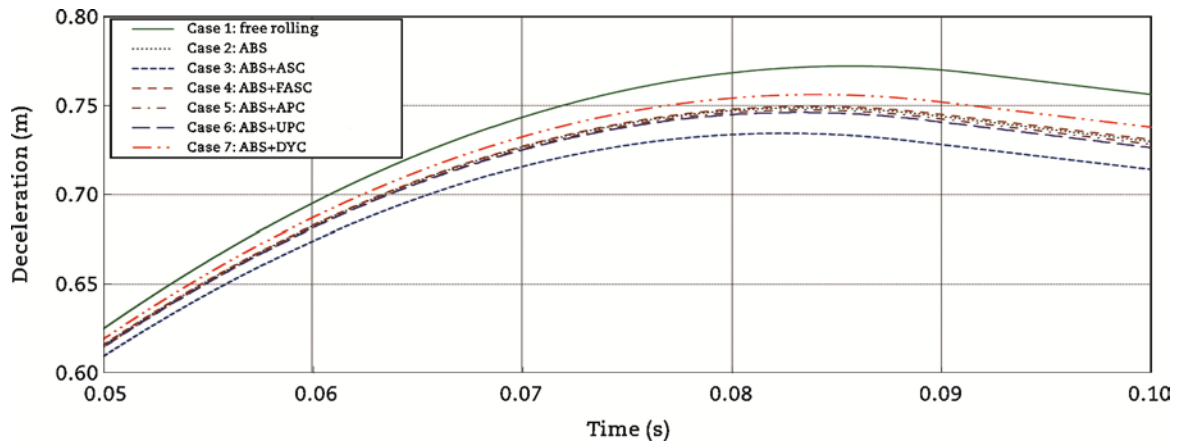


Fig. 11 Deformation of the front-end structure (Offset frontal vehicle-to-vehicle impact).

(a) Vehicle (a). (b) (Enlarge Scale) vehicle (a).

404
405
406

407

408 The deceleration-time histories of the vehicle body for all cases of vehicle (a) are presented in Fig. 12.

409 The deceleration-time history can be divided into three stages. The first stage represents the increase of

410 the vehicle's deceleration before the front left wheel reaches the barrier. In this stage the highest

411 deceleration value is observed in Case 3. In the other cases, a slight higher deceleration is also noticed

412 compared with the free rolling case. In the second stage, the front left wheel reaches the barrier and

413 stop moving, therefore its braking effects is vanished. At the beginning of this stage a rapid reduction in

414 the vehicle body deceleration occurs (arrow 1, Fig. 12). This deceleration drop does not appear in the

415 free rolling case while there is no applied braking. During the second stage, it is noticed that the

416 minimum deceleration is still in Case 1, while the maximum deceleration is almost the same for all other

417 cases. At the end of this stage, the vehicle stops and starts moving in the opposite direction. In addition,

418 the braking force changes its direction and another drop in the vehicle deceleration is noticed as shown

419 in Fig. 12 (arrow 2). At the third stage, a condition of allowing the front-end springs to be rebounded for

420 a very short time is applied during the simulation analysis. During this stage, the vehicle moves back

421 and the deformation of the front-end decreases as shown in Fig. 12. At the end of this stage, the

422 non-linear front-end springs are deactivated and the vehicle's deceleration suddenly dropped to a value

423 of zero. This fast drop is due to the assumption of immediate stopping the effect front-end springs after

424 a very short time of rebound.

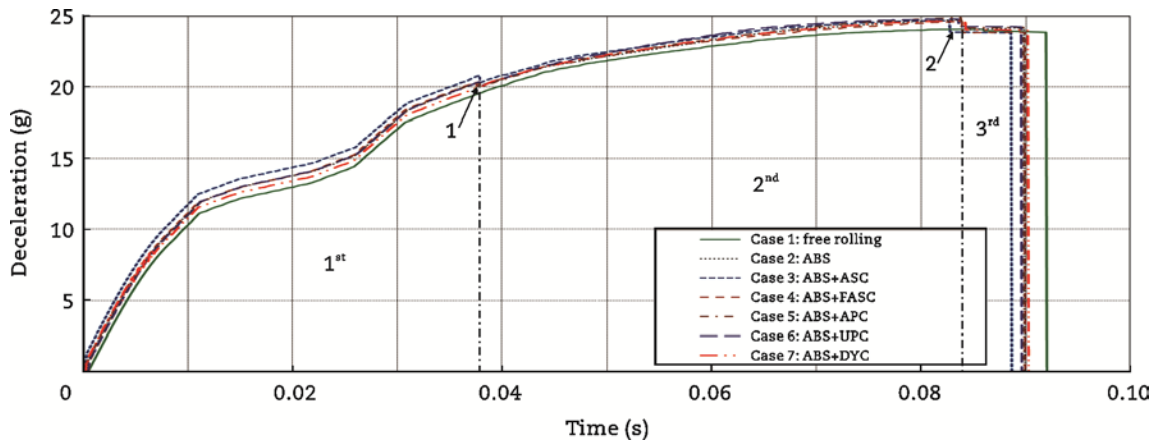
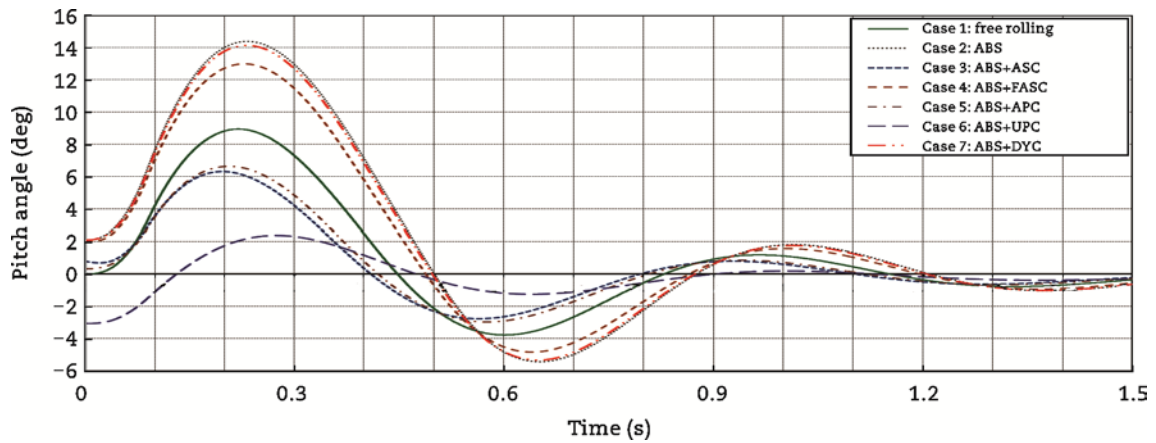


Fig. 12 Vehicle body deceleration (Offset frontal vehicle-to-vehicle impact), vehicle (a).

425
426
427

428 An insignificant increase of the vehicle deceleration in all VDCS cases is observed in the other vehicle
429 (b) compared with the free rolling case. The maximum values of the vehicle deceleration in a vehicle (b)
430 are also almost the same for all the VDCS cases.

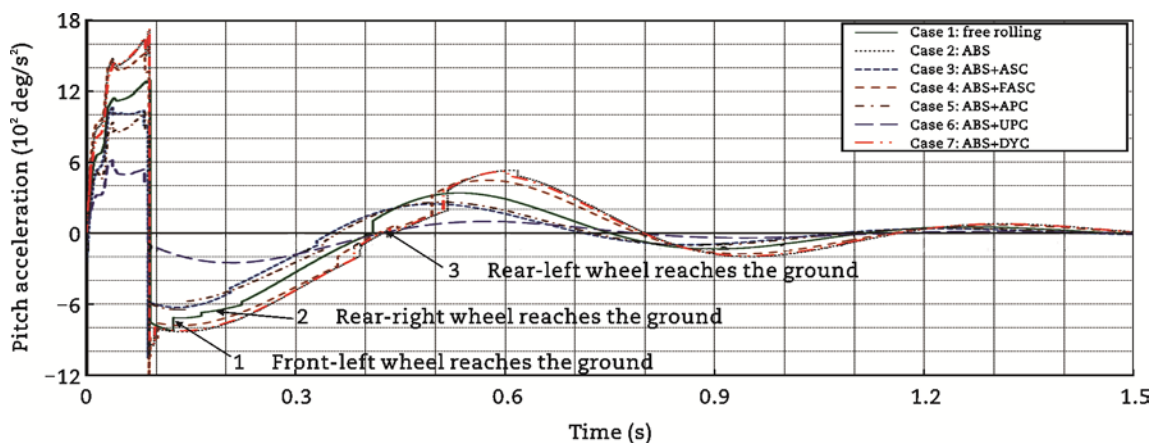
431 Fig. 13 shows the vehicle's pitch angle-time histories for all cases of vehicle (a). The VDCS is applied
432 1.5 s before the collision, therefore, the vehicle body impacts the barrier at different values of pitch
433 angles according to each case as shown in Fig. 13. The vehicle's pitch angle then reaches its maximum
434 values (normally after the end of the crash) according to each case. Following this, the pitch angle
435 reduces to reach negative values and then bounces to reach its steady-state condition. In the offset
436 crash scenario, vehicle body pitching angle is generated due to the difference in impact forces between
437 the upper and lower front-end members of the impacted side in the free rolling case. The additional
438 pitching moment is generated from the braking force in the other VDCS cases. The maximum pitch
439 angle is observed in Case 2 followed by Case 7, 4, 1, 5, 3 and finally Case 6. In Case 6, a notable
440 reduction of about 6.5 deg compared with Case 1 and about 12 deg, compared with Case 2 are
441 observed.



442
443
444 **Fig. 13** Vehicle body pitch angle (Offset frontal vehicle-to-vehicle impact), vehicle (a).

445 A rolling moment of the vehicle body is generated during the crash due to the different values of the
446 component of the left frontal springs' forces in y direction and from the friction between the ground and
447 the tyres due to the yaw motion. At the end of the collision, the pitching and rolling moments are ended
448 and the vehicle is controlled by the tyres and suspension forces. The vehicle's rear wheels left the
449 ground during the vehicle pitching and the left wheels (front and rear) left the ground as well during the
450 vehicle rolling. At this moment, three wheels of the vehicle are not contacted with the ground with
451 different distances. This explains the different sudden changes of the vehicle pitching acceleration when
452 each wheel re-contact the ground (look at the arrows referred to Case 1 in Fig. 14).

453 The vehicle body pitching acceleration is also depicted in Fig. 14 for all seven cases for vehicle (a).
454 The vehicle maximum pitching acceleration is observed in Cases 2, 4 and 7, whilst the lowest value is
455 detected in case 6 (ABS + UPC). Compared with Case 1 (free rolling) and case 2 (ABS), a reduction of
456 about 670 deg/s^2 and about 950 deg/s^2 , respectively, are obtained in Case 6 (ABS + UPC).



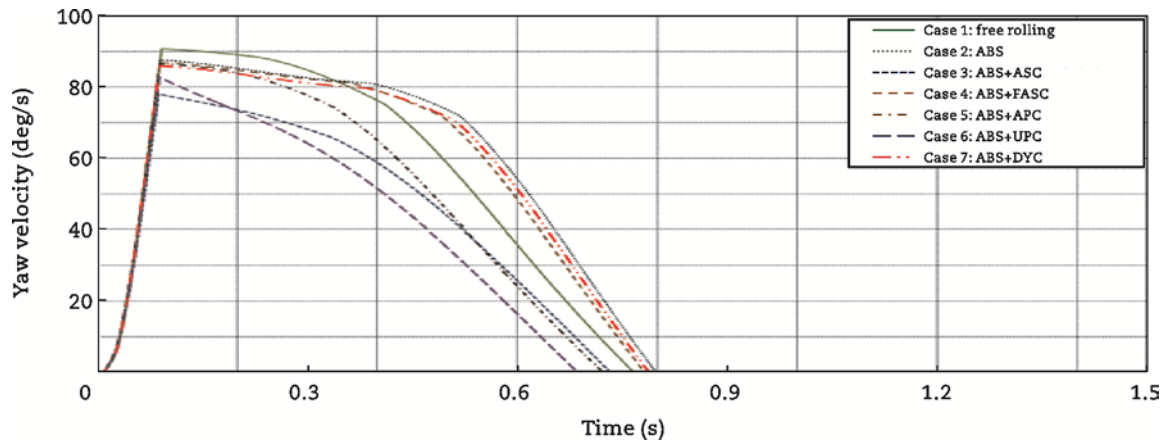
457

458
459

Fig. 14 Vehicle body pitch acceleration (Offset frontal vehicle-to-vehicle impact), vehicle (a).

460 Similarly, the pitch angle and pitch acceleration-time histories for vehicle (b) are obtained. It is noticed
461 that there is no difference between the results of the seven crash scenarios. That means the different
462 applied cases of the VDCS on vehicle (a) do not affect the pitching event of vehicle (b) in case of offset
463 collision.

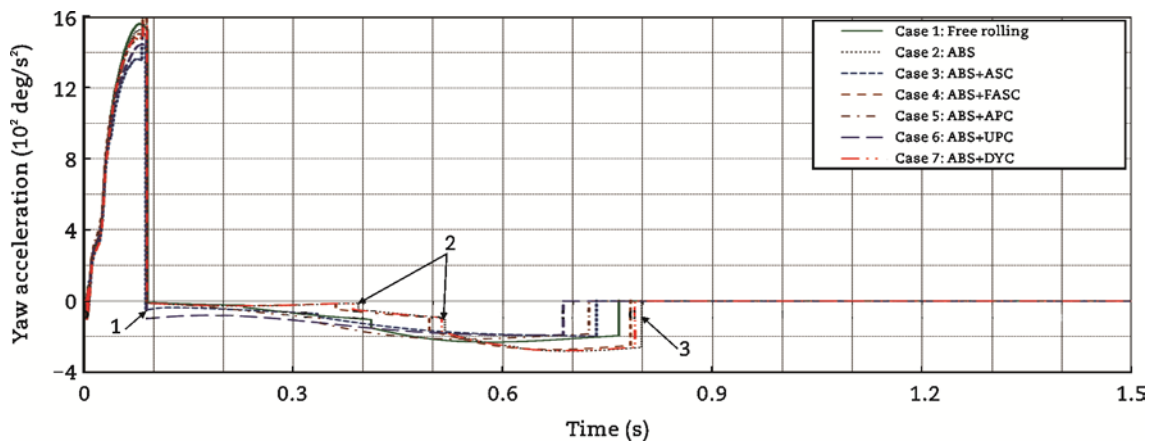
464 Fig. 15 shows the vehicle yaw velocity-time histories for all seven cases of vehicle (a). The vehicle
465 yaw velocity is equal to zero before the crash, then it changes in three different stages: firstly, it
466 increases rapidly to reach its maximum value; secondly, it decreases slowly for a different period of time
467 related to each case; and thirdly it decreases gradually to reach zero. In the first stage, the rapid
468 increase in the yaw velocity is due to the high yawing acceleration (Fig. 16) caused by the one side
469 impacted spring. At the end of the collision, the rear wheels left the ground due to the vehicle pitching
470 and the front-left wheel left the ground due to the vehicle rolling and hence the vehicle is controlled by
471 the front-right wheel only. In the second stage, the decrease in the vehicle's yaw velocity occurred due
472 to the friction force between the front-rear tyre and the ground. The period of this stage is different for
473 each case and it mainly depends on the maximum pitching angle. During the second stage, the front-left
474 wheel re-contacts the ground. Stage 3 begins when the rear wheels start contacting the ground
475 generating yaw moments in the opposite direction. This is causing a reduction of the vehicle yawing
476 velocity with a higher rate than the decreasing of velocity rate in the second stage. Because of the
477 maximum vehicle front-end deformation is observed in Case 1 (free rolling) as shown in Fig. 11, the
478 greatest peak of yaw velocity appears in the same case as shown in Fig. 15. A reduction of the
479 maximum yawing velocity (10 deg/s) is observed in Cases 3 and 6, while a reduction of about 5 deg/s is
480 obtained in the other cases of VDCS.



481
482
483

Fig. 15 Vehicle body yaw velocity (Offset frontal vehicle-to-vehicle impact), vehicle (a).

484 Vehicle body yaw acceleration-time histories are depicted in Fig. 16. The maximum yaw acceleration
485 is observed in Case 1 (free rolling) and the minimum yaw acceleration is also observed in Cases 3 and
486 6. At the end of the collision, the vehicle is controlled by the front-left wheel only, as mentioned before,
487 trying to hinder the yawing motion. Accordingly, a negative yawing acceleration is generated with
488 different small values related to each case as shown in Fig. 16 (arrow 1). These negative values of the
489 vehicle yaw acceleration increase slowly with time producing two sudden drops of acceleration (arrow 2)
490 once the right-rear wheel and the left-rear wheel re-contact the ground, respectively. These drops are
491 not shown in Case 6 because the rear wheels do not leave the ground in this case. When the vehicle
492 yawing ends and the yaw speed reaches zero, the yaw acceleration returns to zero as well as shown in
493 Fig. 16 (arrow 3).

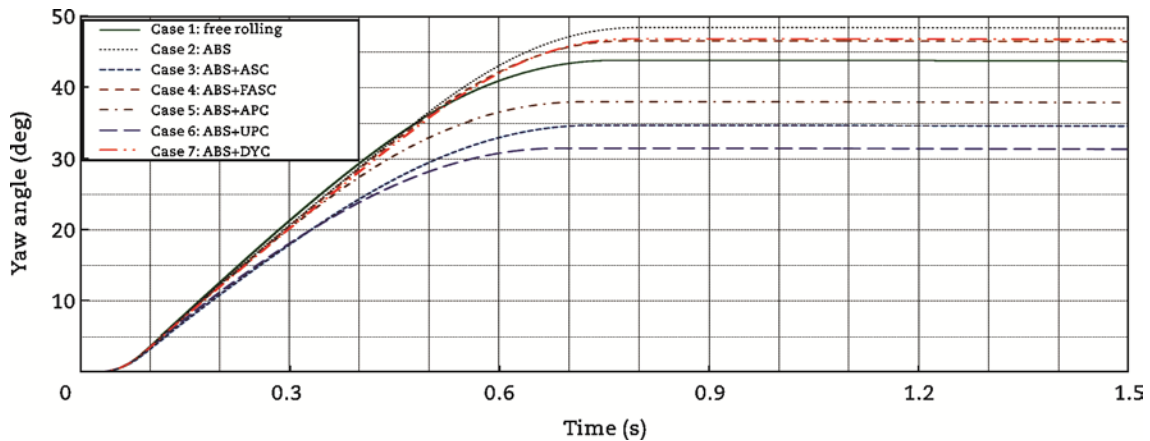


494
495
496

Fig. 16 Vehicle body yaw acceleration (Offset frontal vehicle-to-vehicle impact), vehicle (a).

497 Fig. 17 shows the vehicle body yaw angle-time histories for all cases of vehicle (a). It is found that the

498 maximum yaw angle of 49.3 deg is noticed in Case 2 (ABS) while the minimum yaw angle of 36.8 deg is
 499 noticed in Case 6 (ABS + UPC). The maximum value of the vehicle yaw angle depends on the maximum
 500 yaw acceleration and the vehicle pitch angle for each case. It is worth mentioning that reducing the
 501 maximum vehicle body yaw angle reduces the risk of the car side-impact by any obstacles on the road.
 502 Following the yawing analysis, it can be said that the best set of the vehicle dynamic control is to apply
 503 Case 6 (ABS + UPC) since the minimum yaw angle and acceleration are obtained in this case.



504
 505
 506 **Fig. 17** Vehicle body yaw angle (Offset frontal vehicle-to-vehicle impact), vehicle (a).

507 The yawing event of the vehicle (b), which is not equipped by the VDCS, is affected by vehicle (a)
 508 once different control systems are applied. The maximum yaw velocity of the vehicle (b) is increased in
 509 all cases compared with the free rolling case, except in case 6. It is observed that the maximum yaw
 510 acceleration is also increased in all cases compared with the free rolling case by different values related
 511 to each case. In the same manner, the maximum yaw angle of the vehicle (b) is increased in all cases by
 512 different values (from 1.5 to 2 deg) related to each case, except in case 6. However, all these values are
 513 very small and insignificant.

514 **3.2 Secondary impact results**

515 The secondary impact simulation results for offset vehicle-to-vehicle crash scenario are demonstrated
 516 in this section. The values of different parameters used in numerical simulations are given in Table 2.
 517 The values m_1 , m_2 , m_3 , l_2 , l_3 , k_{12} and k_{23} have been taken from (Ilie and Tabacu, 2010). Fig. 18 shows the
 518 occupant's pelvis relative displacement for vehicle (a). It is shown that it increases forward to reach its

519 maximum position and then returns due to the lower seatbelt springs. It is observed that there are
520 insignificant differences between the values of the maximum relative displacement of the occupant's
521 pelvis. Related to the lower-body deceleration, it is shown that it increases during the collision to reach
522 its maximum values at the end of impact and then reduces after the effect of collision is ended. It
523 observed that the maximum deceleration is almost the same for all cases with very small differences.
524 These small differences mean that the VDACS do have an insignificant effect on the pelvis relative
525 displacement and deceleration.

526

Table 2 Values of the different parameters used in the simulations.

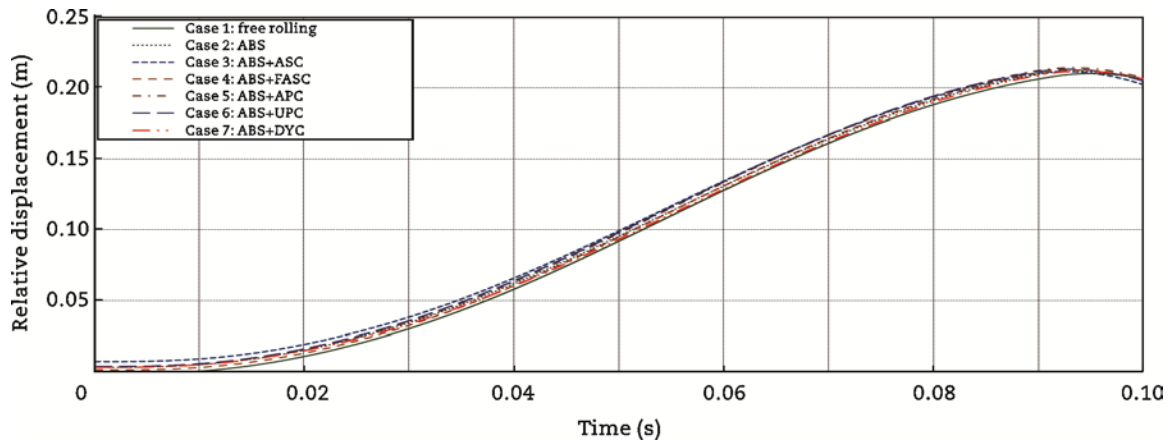
Parameter	m_1	m_2	m_3	l_2	l_3	L_1	L_2	L_3
Value	26.68 kg	46.06 kg	5.52 kg	0.427 m	0.24 m	0.30 m	2.30 m	0.65 m
Parameter	L_4	L_5	L_6	L_7	L_8	L_9	β	ζ
Value	0.3 m	0.35 m	0.45 m	0.55 m	0.97 m	1.1 m	30 deg	15 deg
Parameter	α	γ	ϵ_1	ϵ_2	ρ_1	ρ_2	k_{12}	
Value	23 deg	30 deg	15 deg	15 deg	35 deg	43 deg	380 Nm/rad	
Parameter	k_{23}	k_1	k_2	k_3	k_4	k_5	k_6	
Value	200 Nm/rad	58,860 N/m	39,240 N/m	2500 N/m	2500 N/m	2500 N/m	2500 N/m	
Parameter	$c_1, c_2, c_3, c_4, c_5, c_6$			d_{s1}, d_{s2}	d_{s3}, d_{s4}	d_{s5}	d_{s6}	
Value	20% of the critical damping			0 m	0.05 m	0 m	0.05 m	

527

528 Where d_{s1} , d_{s2} , d_{s3} , d_{s4} , d_{s5} and d_{s6} are the Initial slack lengths of the lower seatbelt, upper seatbelt, lower
529 frontal airbag spring, upper frontal airbag spring, lower side airbag spring and upper side airbag spring,
530 respectively.

531

532



533
534

535 **Fig. 18** Occupant's pelvis displacement (Offset frontal vehicle-to-vehicle impact), vehicle (a).

536

537 The rotation angle of the occupant's chest about y axis for all cases of vehicle (a) is shown in Fig. 19.

538

539 The occupant's chest starts the collision with different rotational angles according to each case. The

540

541 occupant takes this angle in the period of 1.5 s prior collisions when the VDCS is applied. After that, the

542

543 rotational angle of the occupant's chest remains constant for about 0.03 s, then it increased to reach its

544

545 maximum value after the end of the collision. The maximum rotation angle is observed in Cases 2, 4 and

546

547 7 while the minimum one is observed in Case 6 (ABS + UPC). Fig. 20 shows the rotational acceleration

548

about y axis of the occupant's chest. The chest rotational acceleration increases gradually to reach its

549

550 maximum positive value and then reduces to reach its maximum negative value. The maximum positive

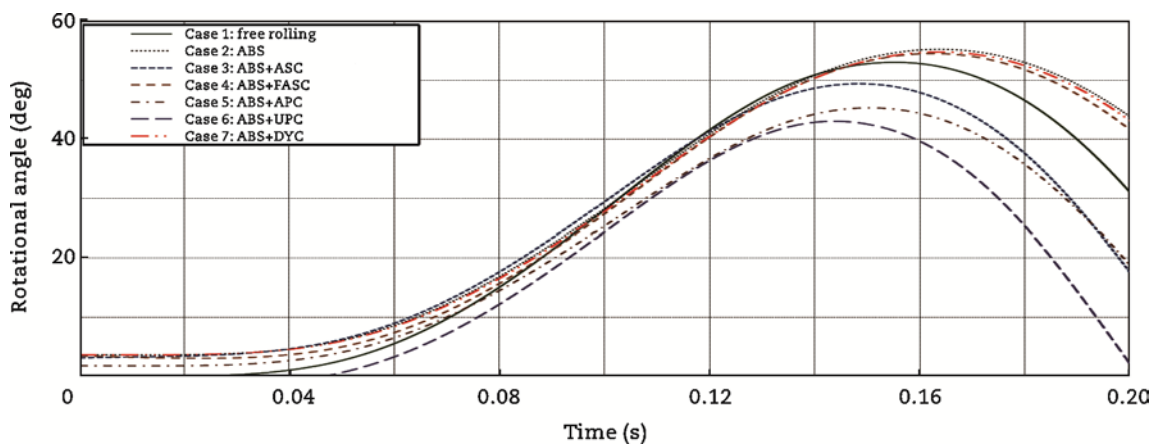
551

552 rotational acceleration is monitored in Case 1 and the minimum one occurred in Case 5, while the

553

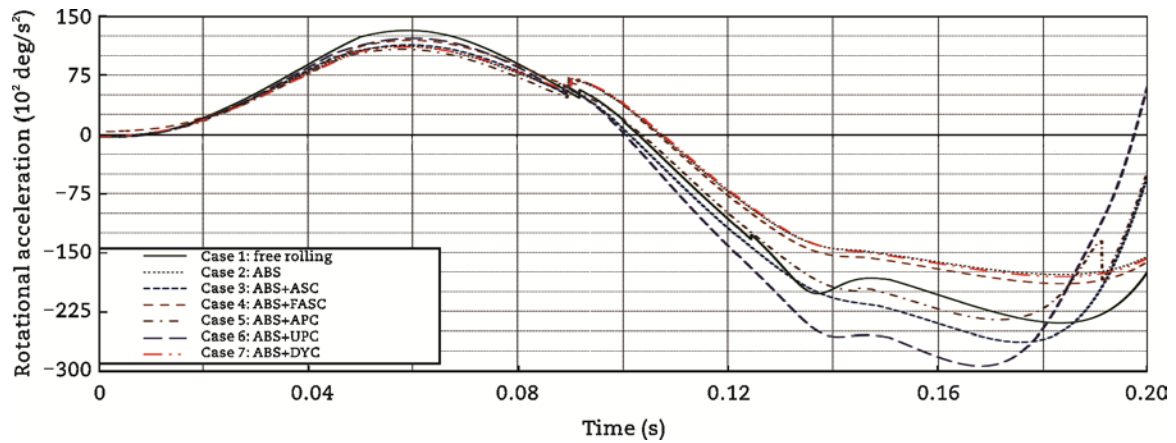
554 maximum negative rotational acceleration is shown in Case 6 and the minimum is in Cases 2 and 7.

555



546
547
548

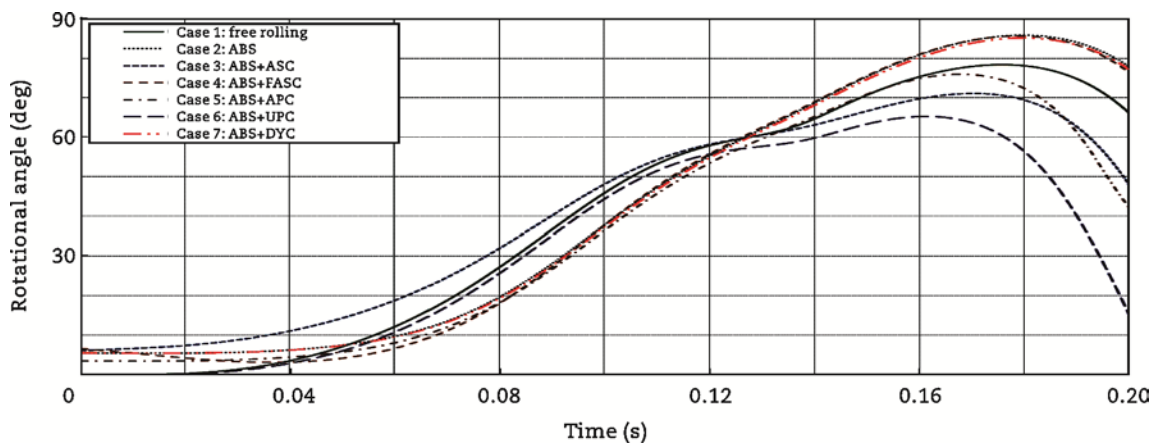
549 **Fig. 19** Rotational angle of the occupant's chest about y axis (Offset frontal vehicle-to-vehicle impact), vehicle (a).



549
550
551

Fig. 20 Rotational acceleration of the occupant's chest about y axis (Offset frontal vehicle-to-vehicle impact), vehicle (a).

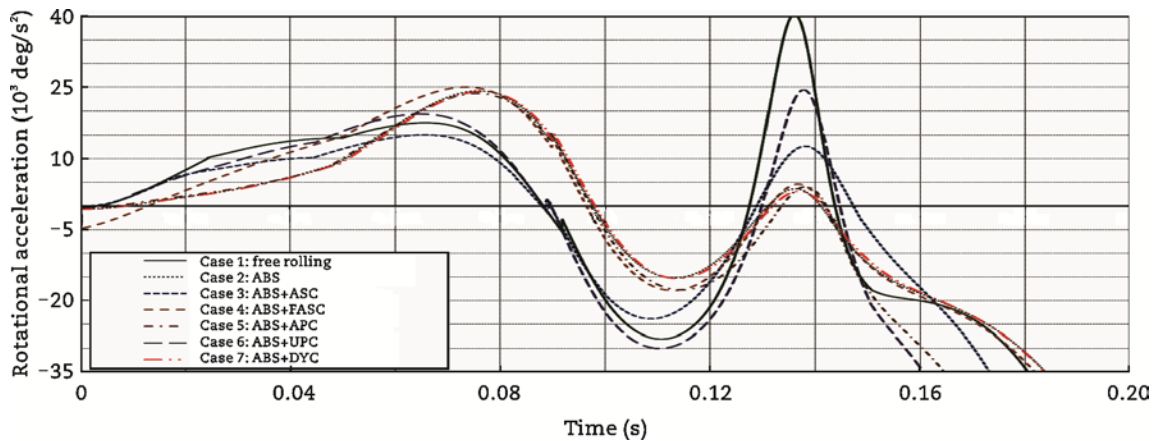
552 The rotation angle of the occupant's head about y axis is depicted in Fig. 21. The head rotation angle
553 increases rapidly for a period of time, which occurred during the increase of the chest rotation. And then,
554 it increases fast due to the return of the occupant's chest to reach its peak value (maximum value). The
555 peak value of the head rotational angle is observed in Cases 2, 4 and 7, while the minimum one is
556 detected in Case 6. Fig. 22 shows the rotational acceleration of the occupant's head. The acceleration
557 increases with a different manner according to each case to reach its maximum value. These maximum
558 values occurred in different time related to each case. In other words, the maximum acceleration in
559 Cases 1, 3 and 6 occurs approximately at 0.07 s, while in the other cases it occurs approximately at 0.08
560 s. The minimum negative acceleration is observed in Cases 2 and 7, while the maximum negative
561 values are seen in Cases 1 and 6.



562
563
564

Fig. 21 Rotational angle of the occupant's head about y axis (Offset frontal vehicle-to-vehicle impact), vehicle (a).

565

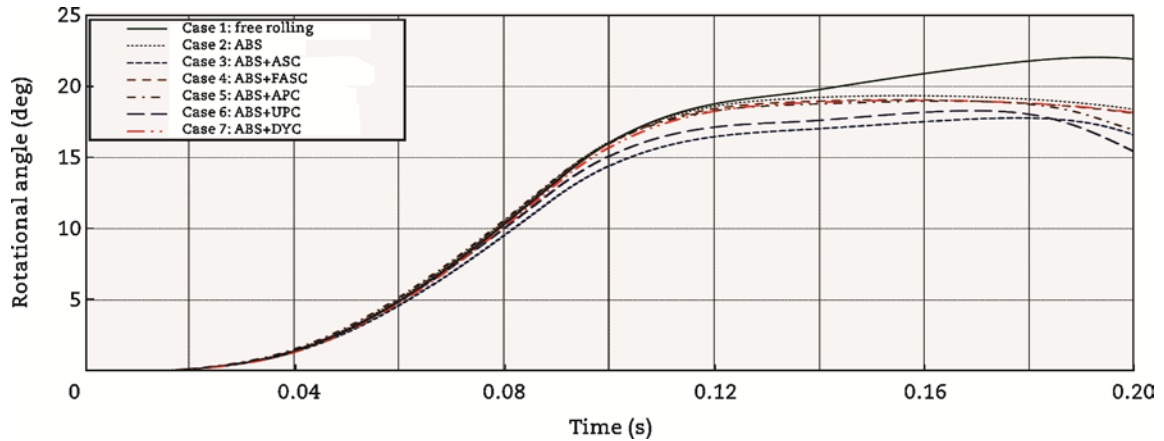


566

567 **Fig. 22** Rotational acceleration of the occupant's head about y axis (Offset frontal vehicle-to-vehicle impact), vehicle (a).

568

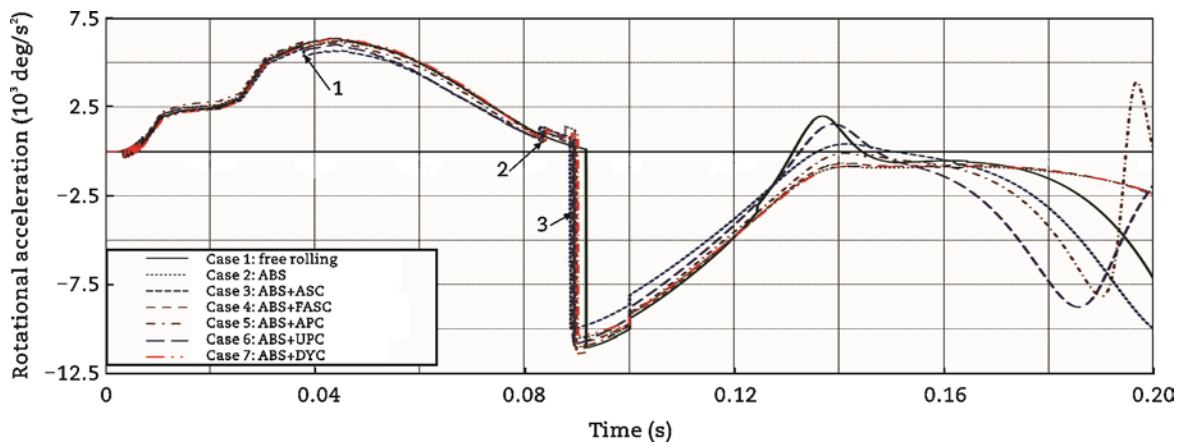
569 The rotation angle about x axis of the occupant's chest for all cases of vehicle (a) is depicted in Fig.
 570 23. When the occupant's chest reaches its maximum rotational angle, it stays in this position for a
 571 period of time while the vehicle rotates around the point of impact. The maximum rotation angle is
 572 observed in Case 1 (free rolling) while the minimum angle is observed in Cases 3 and 6 (ABS + ASC
 573 and ABS + UPC). Fig. 24 shows the rotational acceleration of the occupant's chest about x axis for all 6
 574 cases for vehicle (a). The first sudden change in this acceleration is due to the activation of the side
 575 airbag, while the second one is due to the reverse braking force (arrows 1 and 2, respectively). The third
 576 sudden change of the chest acceleration (arrow 3) is due to the deactivation of the vehicle's front-end
 577 springs, which causes a sudden decrease of the vehicle pitching, yawing and rolling. The maximum
 578 positive rotational acceleration of the occupant's chest about x axis is observed in Cases 1 and 7, while
 579 the minimum value occurs in Case 3. The maximum negative rotational acceleration happens in Cases
 580 1 and 4 and the minimum is observed in Case 3. These negative acceleration values occur due to the
 force generated by the lower spring-damper system of the side airbag.



581
582
583

Fig. 23 Rotational angle of the occupant's chest about x axis (Offset frontal vehicle-to-vehicle impact), vehicle (a).

584



585
586

Fig. 24 Rotational acceleration of the occupant's chest about x axis (Offset frontal vehicle-to-vehicle impact), vehicle (a).

587

588

589

590

591

592

593

594

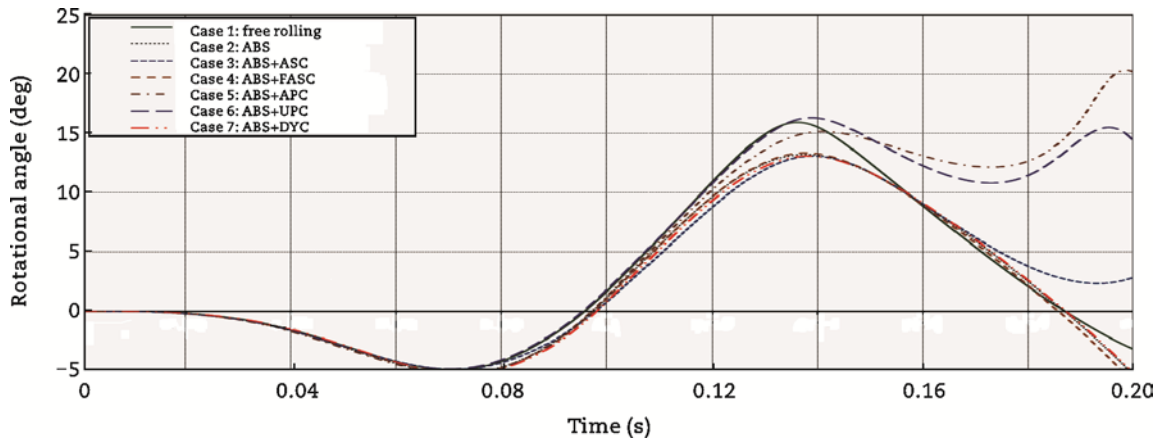
595

596

597

The rotation angle about x axis of the occupant's head for vehicle (a) is shown in Fig. 25. At the beginning of the collision, while the chest takes a positive acceleration and starts rotating towards the vehicle's side door, the head takes a different negative small rotation value related to each case, all these values are close to 5 deg. The positive maximum value of the head rotational angle is observed in Case 6, while the minimum peak angle is seen in Cases 2, 3, 4 and 7. Fig. 26 shows the rotational acceleration about x axis of the occupant's head for all cases. The effect of the reverse braking force is observed at the end of the collision (arrow 1 in Fig. 26). The maximum positive acceleration (in the period from 0.06 to 0.10 s) is almost the same for all cases, while the maximum negative acceleration (in the period from 0.10 to 0.16 s), caused by the side airbag force, is observed in Case 1 with relatively a higher value. The minimum negative acceleration is detected in Cases 2, 4, 5 and 7.

598

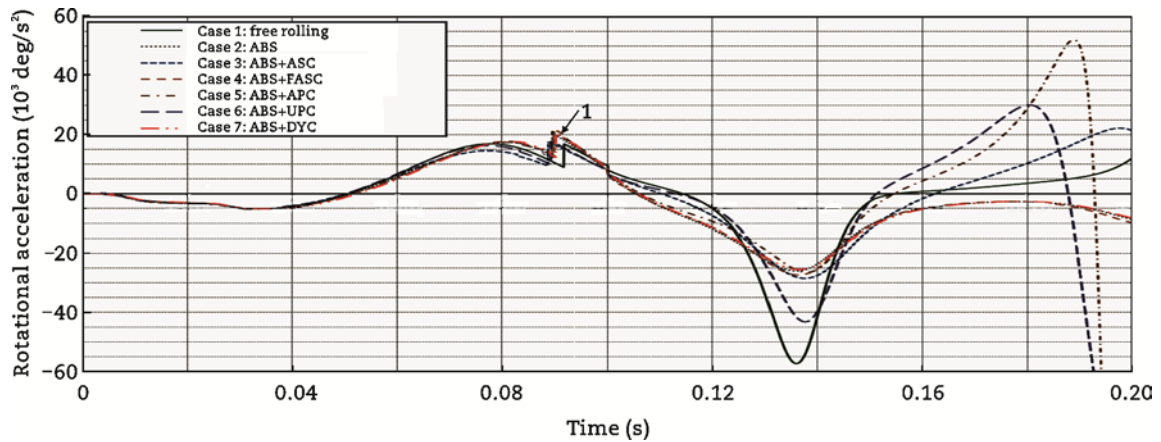


599
600

601

Fig. 25 Rotational angle of the occupant's head about x axis (Offset frontal vehicle-to-vehicle impact), vehicle (a).

602



603
604

605

Fig. 26 Rotational acceleration of the occupant's head about x axis (Offset frontal vehicle-to-vehicle impact), vehicle (a).

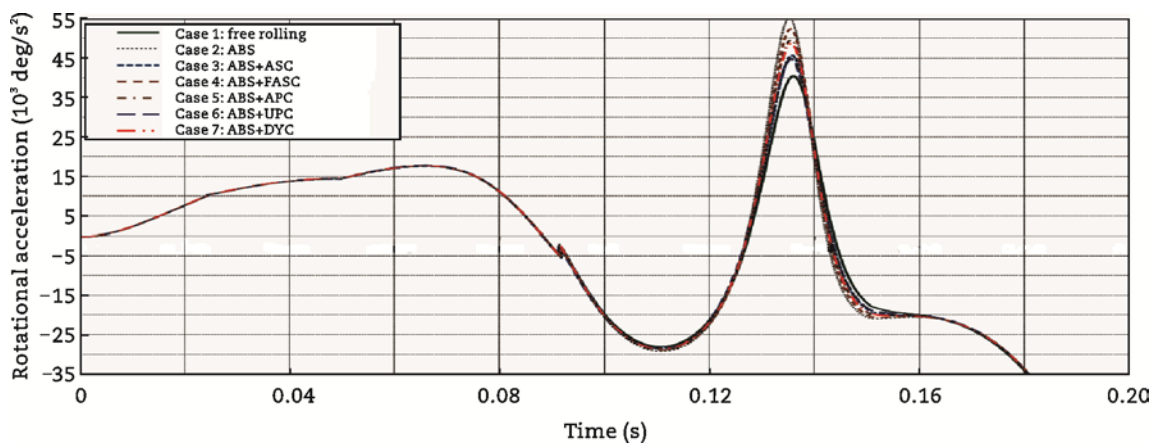
606

607 It is shown that the occupant's pelvis relative displacement and deceleration for vehicle (b) are
608 insignificantly affected by the application of VDCS on the other vehicle (vehicle (a)). There are very
609 small and insignificant increases, especially on the peak values, for all cases compared with the free
610 rolling case.

611 The occupant's chest rotational angle for vehicle (b) and its acceleration about y axis are also
612 obtained. It observed that there are no changes in the rotational angle; however, there are small
613 variations among the different cases on the occupant's chest acceleration from 0.13 to 0.15 s. These
614 variations are also very small and insignificant.

615 The occupant's head rotational angle about y axis for the occupant in vehicle (b) is gained. It is shown
 616 that there are very small differences of the maximum rotational angle according to the different cases.
 617 Fig. 27 shows the occupant's head rotational acceleration about y axis for all cases. From this figure, a
 618 clear difference in the head rotational acceleration is detected at 0.135 s. When the VDCS is applied,
 619 the maximum head rotational acceleration becomes higher than the one in the free rolling case with
 620 different values from 5 to 15 kdeg/s^2 related to each case; and the maximum head rotational
 621 acceleration is shown in case 2.

622



623
624

625 **Fig. 27** Rotational acceleration of the occupant's head about y axis (vehi Offset frontal vehicle-to-vehicle impact), vehicle (b).

626 The occupant's chest rotational angle about x axis for vehicle (b) is recorded. Compared with the free
 627 rolling case, the rotational angle of the chest is increased by small values from about 0.2 deg in Case 6
 628 to about 2 degs in Cases 2 and 4. The occupant's chest acceleration about the x axis showed very small
 629 increases of the chest rotational acceleration when the VDCS are applied at the periods from 0.04 to
 630 0.09 s and from 0.13 to 0.15 s. This increase in the chest rotational acceleration ranges between 300 to
 631 800 deg/s^2 , however, these are not significant values.

632 The maximum occupant's head rotational angle about x axis is also increased when any of the VDCS
 633 is applied. This increase ranges between 0.2 to 1.0 deg, and this is not a significant value. The
 634 maximum head rotational angle is observed in Case 2, while the minimum value is detected in Case 1.
 635 The maximum positive acceleration of the occupant's head about x axis is almost the same. However,
 636 the maximum negative head rotational acceleration is increased when the VDCS are applied. In Case 6

637 the head rotational acceleration is increased by about 5 kdeg/s², while the highest increase value is
638 observed in Case 2 by about 15 kdeg/s².

639 **4 Conclusions**

640 Development of a new 6-DOF vehicle dynamics/crash mathematical model and three
641 dimensional-three-mass occupant mathematical model have been represented to study the effect of
642 vehicle dynamic control systems (VDCS) on vehicle crash at offset frontal vehicle-to-vehicle collision.
643 The models presented here would be very useful in the early design stages for assessing the crash
644 worthiness performance of the vehicle and for selecting appropriate vehicle parameters. From the
645 numerical simulations, it can be said that the VDCS can improve the vehicle crash situation and the
646 occupant behaviour. The different cases applied in this paper have a different effect on the vehicle and
647 its occupant. It is shown that the crash event gets worse related to the vehicle (b), based on higher
648 values of vehicle deceleration, pitching angle and acceleration, etc. However, these higher values are
649 very small and insignificant

650 **Acknowledgments**

651 The authors would like to thank the Egyptian government and the Faculty of Engineering, Ain Shams
652 University for supporting this research. We also acknowledge with sadness, the contribution of Prof.
653 Dave Crolla who has passed away during the period of this research.

654
655
656
657
658
659
660
661

662 **References**

663 Alleyne, A., 1997. Improved vehicle performance using combined suspension and braking forces.
664 Vehicle System Dynamics 27(4), 235–265.

665 Alleyne, A., Hedrick, J.K., 1995. Nonlinear Adaptive Control of Active Suspensions. IEEE Transactions
666 on Control Systems Technology, 3, 1, pp. 94 –101.

667 Bang, M.S., Lee, S.H., Han, C.S., et al., 2001. Performance enhancement of a sliding mode wheel slip
668 controller by the yaw moment control. Proceedings of the Institution of Mechanical Engineers Part
669 D: Journal of Automobile Engineering 215(4), 455–468.

670 Celentano, G., Iervolino, R., Porreca, S., et al., 2003. Car brake system modeling for longitudinal control
671 design. In: IEEE Conference on Control Applications, USA, 2003.

672 Chang, J.M., Ali, M., Craig, R., et al., 2006. Important Modeling Practices in CAE Simulation for Vehicle
673 Pitch and Drop. SAE International, Warrendale.

674 Elkady, M., Elmarakbi, A., 2012. Modelling and analysis of vehicle crash system integrated with different
675 VDCS under high speed impacts. Central European Journal of Engineering 2(4), 585-602.

676 Elmarakbi, A., Elkady, M., MacIntyre, J., 2013. Numerical analysis of vehicle-to-vehicle impact using
677 vehicle dynamics control systems for collision mitigation. International Journal of Dynamics and
678 Control 1(2),172-191.

679 Elmarakbi, A., Zu, J., 2005. Crashworthiness improvement of vehicle-to-rigid fixed barrier in full frontal
680 impact using novel vehicle's front-end structures. International Journal of Automotive Technology
681 6(5), 491-499.

682 Elmarakbi, A., Zu, J., 2007. Incremental harmonic balance method for analysis of standard/smart
683 vehicles-to-rigid barrier frontal collision. International Journal of Vehicle Safety 2(3), 288-315.

684 Emori, R.I., 1968. Analytical Approach to Automobile Collisions. SAE International, Warrendale.

685 Gietelink, O., Ploeg, J., De Schutter, B., et al., 2006. Development of advanced driver assistance
686 systems with vehicle hardware-in-the-loop simulations. International Journal of Vehicle Mechanics
687 and Mobility 44(7), 569–590.

688 Hogan, I., Manning, W., 2007. The use of vehicle dynamic control systems for automotive collision
689 mitigation. In: The 3rd Institution of Engineering and Technology Conference on Automotive
690 Electronics, USA, 2007.

691 Ilie, S., Tabacu, Ş., 2010. Study of the Occupant's Kinematics during the Frontal Impact. Ann Oradea
692 University, Fascicle Management Technology Engineering 6(16), 542–551.

693 Jansson, J., Gustafsson, F., Ekmark, J., 2002. Decision Making For Collision Avoidance Systems. SAE
694 International, Warrendale.

695 Kamal, M.M., 1970. Analysis and Simulation of Vehicle to Barrier Impact. SAE International,
696 Warrendale.

697 Khattab, A., 2010. Steering System and Method for Independent Steering of Wheels (PhD thesis).
698 Concordia University Montreal, Quebec.

699 Kim, H.S., 2002. New Extruded Multi-Cell Aluminum profile for maximum crash energy absorption and
700 weight efficiency. Thin-Walled Structures 40(4), 311–327.

701 Ori, T.R., Gbaha, P., Asseu, O., et al., 2011. Vehicle stopping distance by means of suspensions
702 control. Asian Journal of Scientific Research 4(1), 28-41.

703 Pasillas-Lépine, W., 2006. Hybrid modeling and limit cycle analysis for a class of five-phase anti-lock
704 brake algorithms. Vehicle System Dynamics 44(2), 173–188.

705 Seiler, P., Song, B., Hedrick, J., 1998. Development of a Collision Avoidance System. SAE International,
706 Warrendale.

707 Sugimoto, Y., Sauer, C., 2005. Effectiveness estimation method for advanced driver assistance system
708 and its application to collision mitigation brake system. In: The 19th International Technology
709 Conference on the Enhanced Safety Vehicles, Washington DC, 2005.

710 Tamura, M., Inoue, H., Watanabe, T., et al., 2001. Research on a Brake Assist System with a Preview
711 Function. SAE International, Warrendale.

712 Witteman, W.J., 1999. Improved Vehicle Crashworthiness Design by Control of the Energy Absorption
713 for Different Collision Situations (PhD thesis). Eindhoven University of Technology, Eindhoven.

714 Witteman, W.J., Kriens, R.F.C., 1998. Modeling of an innovative frontal car structure: similar
715 deceleration curves at full overlap, 40 percent offset and 30 degrees collisions. In: 16th
716 International Technical Conference on the Enhanced Safety of Vehicles, Windsor, 1998.

717 Yu, F., Feng, J.Z., Li, J., 2002. A fuzzy logic controller design for vehicle abs with an on-line optimized
718 target wheel slip ratio. International Journal of Automotive Technology 3(4), 165–170.

719 Yue, C., Butsuen, T., Hedrick, J.K., 1988. Alternative Control Laws for Automotive Active Suspensions.
720 Journal of Dynamic Systems, Measurement, and Control 111(2), 286-291.

721
722
723
724
725



726

727 **Mustafa Elkady** is an assistant professor of mechanical engineering at Lebanese International
728 University (LIU). He received a competition grant from the Egyptian government (~ £100,000 -3 years)
729 for his PhD. He obtained his PhD in mechanical engineering at the Department of Computing,
730 Engineering and Technology, University of Sunderland, UK (2012). Prior to this he was a teaching
731 assistant in mechanical engineering at the Automotive Department, Ain Shams University, Egypt. He
732 obtained his Master degree in automotive engineering at Ain Shams University, Egypt (2004). Prior to
733 this he was a demonstrator in mechanical engineering at the Automotive Department, Ain Shams
734 University. His research interests include mathematical modeling analysis, advanced dynamics, vehicle
735 dynamics, crashworthiness, vehicle safety and impact biomechanics, vehicle engine controls and
736 energy-efficient using lightweight materials. His research outcomes are realized as evident from his
737 over 20 publications, he has published the book, Enhancement of Vehicle Crash/Occupant Safety:
738 Mathematical Modelling.

739
740
741
742



743

744 **Ahmed Elmarakbi** obtained his PhD in mechanical engineering from the University of Toronto, Canada
745 (2004). After successful postdoctoral fellowships in Canada and Japan, he moved to the University of
746 Sunderland, UK in 2007, where he is, currently, professor of automotive composites. His research
747 interests lie in the area of energy-efficient and safe vehicles (EESVs) including advanced composite
748 materials (e.g. grapheme) for automotive applications and low carbon vehicles. His work outcomes are
749 recognised both nationally and internationally as evident from his 70+ plenary lectures, invited talks and
750 presentations; 130+ peer-reviewed research papers. Most recently (2013), he has published the book:
751 Advanced Composite Materials for Automotive Applications: Structural Integrity and Crashworthiness,
752 with Wiley, UK. He has 15 years of experience managing national and international projects, including
753 multi-disciplinary collaborative projects with Europe, USA, Canada, China, Japan, and Brazil. He has
754 received many prestigious awards and grants world wide, including EU Graphene Flagship,
755 Horizon2020, EPSRC, NSERC, JSPS, OGS, FP7, and several fellowships. He is expert reviewer for
756 FP7 and EPSRC, member of several professional bodies; editorial-board member of high-impact
757 international journals; organiser of international conferences and reviewer for conferences and many
758 high-impact journals. He is also founder Editor-in-Chief of International Journal of Automotive
759 Composites. He has an extensive track record of collaboration with the automotive industry and
760 world-class academic institutions over the last 15 years and he is currently a member of the EU
761 Graphene Flagship.

762

763

764

765

766



767

768 **John MacIntyre** is the dean of the Faculty of Applied Sciences, and Pro Vice Chancellor at the
769 University of Sunderland. He has worked at the University of Sunderland since 1992, having graduated
770 from the University with a First Class Honours Degree in combined science (computer science and
771 physiology). He then went on to complete a PhD in applied artificial intelligence, focussing on the use of
772 neural networks in predictive maintenance, which was awarded in 1996. During 1990s John established
773 a research centre for adaptive systems at the university, which became recognised by the UK
774 government as a centre of excellence for applied research in adaptive computing and artificial
775 intelligence. The centre undertook many projects working with and for external organisations in industry,
776 science and academia, and for three years ran the smart software for decision makers programme on
777 behalf of the Department of Trade and Industry. He has successfully supervised PhDs in fields ranging
778 from neural networks, hybrid systems, and bioinformatics through to lean manufacturing, predictive
779 maintenance, and business and maintenance strategies. He went on to become associate dean, and
780 then the dean of the School of Computing, Engineering and Technology, covering computer science
781 and engineering. In 2008 he became the dean of the Faculty of Applied Science, and in 2010 Pro Vice
782 Chancellor of the University.



783

784 **Mohammad Alhariri** is research assistant in the Department of Computing, Engineering and
785 Technology and a PhD student in automotive engineering in the University of Sunderland. His research
786 interests lie in the area of safety in passenger-vehicle. His current work focuses on developing a novel
787 controller for vehicles dynamic systems aiming for better energy absorption resulting from vehicle frontal
788 crashes.